Check for updates

Received: 29 April 2026 | Revised: 11 August 2026 | Accepted: 19 August 2026

DOI: 10.1002/qj.70305

Quarterly Journal of the Royal Meteorological Society RMetS

RESEARCH ARTICLE

Multi-scale flow analysis for scale-aware urban canopy models

Jingzi Huang | **Maarten van Reeuwijk**

Department of Civil and Environmental Engineering, Imperial College London, London, UK

Correspondence
Jingzi Huang, Department of Civil and Environmental Engineering, Imperial College London, London, SW7 2AZ, UK.
Email: jingzi.huang17@imperial.ac.uk

Funding information
Natural Environment Research Council, Grant/Award Number: NE/W002868/1; ARCHER Service, Grant/Award Number: ARCHER2-eCSE05-3

Abstract

As numerical weather prediction (NWP) models approach hectometric resolution, they operate increasingly in a regime where urban heterogeneity, specifically the morphological heterogeneity and resulting flow heterogeneity, is only partially resolved and the assumptions underlying conventional urban canopy models (UCMs) become questionable. To address this scale gap, we apply the multi-scale coarse-graining framework to building-resolving large-eddy simulations (LES) of the University of Bristol campus, a realistic heterogeneous urban environment. Two related morphologies are considered: an original layout containing large open-space contrasts and a modified configuration with these regions infilled. By filtering the LES fields systematically, we quantify how flow heterogeneity is partitioned between resolved and unresolved contributions as the averaging length changes and identify a characteristic urban length-scale ℓ of flow heterogeneity at which resolved and unresolved variability are comparable. This scale is strongly morphology-dependent, with $\ell \approx 256\,\mathrm{m}$ for the original layout and $\ell \approx 64\,\mathrm{m}$ for the modified case, demonstrating that neighbourhood-scale organisation can remain dynamically important at resolutions relevant to next-generation NWP. Using this framework, we perform an a priori assessment of distributed drag and turbulent-stress parameterisations. The results show that parameterisations derived from idealised geometries perform reasonably well only at sufficiently large averaging length-scales ($L \gtrsim \ell$, corresponding to coarse resolutions), where horizontal transport is negligible and the flow appears approximately homogeneous. At smaller averaging lengths, their fidelity degrades rapidly due to increasing heterogeneity and filter-to-filter variability in morphology. These limitations are more pronounced in realistic layouts than in idealised cuboid arrays. Overall, the results highlight that the applicability of urban parameterisations depends critically on the relationship between model resolution and the characteristic urban length-scale of morphology-dependent flow heterogeneity. The framework provides a systematic route to diagnose this scale and to guide the development of scale-aware urban canopy models for high-resolution NWP.

KEYWORDS

drag parameterisation, heterogeneity, large-eddy simulation, multi-scale analysis, urban canopy

This is an open access article under the terms of the Creative Commons Attribution License, which permits use, distribution and reproduction in any medium, provided the original work is properly cited.
© 2026 The Author(s). *Quarterly Journal of the Royal Meteorological Society* published by John Wiley & Sons Ltd on behalf of Royal Meteorological Society.

1 | INTRODUCTION

Over recent decades, the resolution of numerical weather prediction (NWP) models has increased to kilometre or even hectometre scales, enabling the models to resolve key atmospheric processes such as convection (Baldauf *et al.*, 2011; Bryan *et al.*, 2003; Tang *et al.*, 2013). Nevertheless, it remains challenging for NWP models to capture the key processes within the urban canopy layer (UCL). The UCL is characterised by strong urban heterogeneity, where two closely coupled aspects are central: morphological heterogeneity, arising from spatial variation in buildings, street canyons, vegetation, and neighbourhood-scale organisation (typically at $\mathcal{O}$(100–500 m)), and flow heterogeneity, defined as spatial variability in wind, turbulence, and transport. The morphological heterogeneity provides the principal forcing that generates the flow heterogeneity, particularly under neutral conditions. Consequently, urban canopy models (UCMs) represent subgrid-scale processes within the UCL by parameterising unresolved interactions between the atmosphere and the urban land surface.

Different levels of UCMs have been developed, ranging from single-layer schemes (Kanda *et al.*, 2005; Kusaka *et al.*, 2001; Lipson *et al.*, 2024) based on bulk parameters such as roughness lengths, displacement heights, and plan-area indices to multiple-layer schemes (Coceal & Belcher, 2004; Martilli *et al.*, 2002) that classify the UCL into vertical sub-layers according to the distribution of building heights and vegetation, and more recently to refined vertically distributed schemes that represent the evolution of momentum and heat with height (Lu *et al.*, 2024; Sützl *et al.*, 2021). However, conventional UCMs generally do not account explicitly for subgrid-scale variance. Single-layer schemes represent urban morphology using bulk morphological indices and therefore neglect within-cell morphological heterogeneity. Multiple-layer schemes resolve vertical variations but typically assume that exchange is dominated by vertical transport, thereby neglecting the resulting horizontal flow heterogeneity and associated horizontal flux divergences within the grid cell. These assumptions increasingly break down as NWP grid spacing approaches O(1 km) and below, where neighbourhood-scale morphological heterogeneity, such as clusters of tall buildings, open squares, and variations in street orientation, strongly modulates momentum transport, turbulence generation, and scalar dispersion (Masson *et al.*, 2020; Stewart & Oke, 2012). Hectometric NWP models help address this issue by partially resolving key physical processes, particularly boundary-layer turbulence, which improves predictions of near-surface winds and turbulence kinetic energy in urban areas by up to 30% compared with coarser models (Lean *et al.*, 2024). However, at these scales, the urban surface enters the so-called *building grey zone*, in which morphological heterogeneity associated with large buildings becomes important, and the resulting flow around them is represented partly at the grid scale and partly at the subgrid scale. Therefore, the parameterisations become more complex and horizontal exchanges between adjacent grid cells become first-order (Lean *et al.*, 2024). Chen and Dipankar (2022) demonstrated that the homogeneous-building assumption in conventional UCMs can break down in the sub-kilometre building grey zone, highlighting the need to diagnose scale-dependent urban heterogeneity. Ultimately, to resolve this problem, it becomes necessary to relax the UCM assumption of horizontal flow and morphological homogeneity and to develop scale-aware models, which are adjusted according to changes in model resolution (Barlow, 2014). Correspondingly, an analysis framework is required to develop and evaluate such models systematically across a range of scales.

To address these cross-scale challenges, the UK Across-Scale processeS in URban Environments (ASSURE) project, which is funded by the Natural Environment Research Council (NERC), provides an integrated framework combining field observations, high-fidelity numerical simulations, and controlled wind-tunnel experiments. Focusing on the city of Bristol, characterised by complex topography and diverse urban morphology, ASSURE aims to determine which urban processes must be resolved explicitly and which require parameterisation in next-generation models. The project integrates city-scale measurements (Ludwig *et al.*, 2025), multi-source tracer experiments and Direct Numerical Simulation (Auerswald *et al.*, 2024; Clements *et al.*, 2024), building-resolving large-eddy simulations (LES: Coburn *et al.*, 2022; van Reeuwijk & Huang, 2025b), and atmospheric boundary layer (ABL) wind-tunnel experiments (Ding *et al.*, 2023) at the Surrey Environmental Flow Laboratory (EnFlo). The project provides a systematic basis for quantifying the evolution of urban flow and transport across scales.

As part of this effort, van Reeuwijk and Huang (2025b) developed a multi-scale analysis framework that bridges the scale gap between the high-resolution LES and spatial-average-based UCMs and therefore provides a systematic way to examine how urban flow statistics and model performance evolve with resolution. Relying on a coarse-graining method applied to building-resolving simulations, this framework identifies a characteristic urban length-scale of morphology-induced flow heterogeneity at which the resolved and unresolved contributions to flow variance are equally important. In the framework, the flow heterogeneity is the quantity diagnosed, whereas the

1477870x, 0, Downloaded from https://rmets.onlinelibrary.wiley.com/doi/10.1002/qj.70305 by Imperial College London, Wiley Online Library on [25/09/2026]. See the Terms and Conditions (https://onlinelibrary.wiley.com/terms-and-conditions) on Wiley Online Library for rules of use; OA articles are governed by the applicable Creative Commons License

morphological heterogeneity, characterised by variations in building height, plan-area, and frontal-area indices, provides the underlying forcing that generates the flow heterogeneity. Moreover, the framework enables an a priori diagnosis of urban drag and turbulence parameterisations using only morphological input. However, like many fundamental urban studies (Coceal & Belcher, 2004; Macdonald *et al.*, 1998; van Reeuwijk & Huang, 2025b; Xie *et al.*, 2008) applied the framework to an idealised geometry. Although idealised geometries provide fundamental insights, they lack the morphological heterogeneity and complexity of real cities. Even within idealised cube and cuboid arrays, Blunn *et al.* (2022) found that fundamental closure parameters such as the von Kármán coefficient vary between approximately 0.20 and 0.51 across geometries, and that the mixing-layer analogy borrowed from vegetation canopies does not transfer to urban canopies, because shear is local to individual buildings rather than dominated by a single canopy-top scale. Studies on realistic urban geometries have shown that the effective drag and mixing lengths are likewise not governed by a single length-scale, but by a superposition of scales arising from individual buildings, street canyons, and district-level clustering (Cheng & Yang, 2023). Such findings highlight the limitations of extrapolating idealised parameterisations to real-world conditions and underscore the need to incorporate realistic geometry into multi-scale analyses (Kusaka *et al.*, 2024).

The purpose of this study is to apply the multi-scale framework of van Reeuwijk and Huang (2025b) to a realistic urban environment and investigate how urban heterogeneity evolves with scale and how subgrid-scale variability emerges as resolution is reduced on realistic morphology. Specifically, we aim (i) to investigate the characteristic urban length-scale of flow heterogeneity induced by complex real morphologies and (ii) to assess, in an a priori sense, the performance of distributed drag and turbulent-stress parameterisations over realistic morphologies. This is particularly important because, in contrast to uniform idealised layouts, the performance of such parameterisations is expected to vary more strongly across length-scales in realistic, highly non-uniform configurations. Ultimately, this work offers new insights into the resolution-aware representation of realistic urban processes for NWP models. To address these questions, high-resolution LES are performed for the University of Bristol campus—one of the main focus sites of the ASSURE project, which is characterised by strong heterogeneity in building shapes, a wide range of orientations, and large variations in building height.

The article is organised as follows. Section 2 reviews the multi-scale framework developed in van Reeuwijk and Huang (2025b). Section 3 details the simulations and the two realistic morphological layouts. Results are presented in Section 4, comprising both a conventional plane-averaged analysis and the novel multi-scale analysis. Conclusions are drawn in Section 5.

2 | MULTI-RESOLUTION PLANAR-AVERAGING FRAMEWORK FOR URBAN CANOPY FLOWS

In this section, we review the computationally efficient multi-resolution planar-averaging framework of van Reeuwijk and Huang (2025b). The framework uses convolution filters to derive coarse-grained fields from a building-resolved high-resolution field. This approach provides a systematic means to conduct a multi-scale analysis of urban canopy flow. By applying the framework, we then introduce the planar-averaged drag and kinematic stresses and their parameterisations, which will be examined later through an a priori analysis.

2.1 | Planar averaging with convolution filters

Consider a 3-D urban domain of interest Ω that is divided into a fluid subdomain Ω_f and a solid subdomain Ω_b, separated by the fluid–solid interface $\partial\Omega_\mathrm{f}$ (Figure 1). The coarse-graining method computes the *superficial* planar average of an arbitrary field φ over a square horizontal filter of length-scale L, as illustrated in Figure 1a,b. Mathematically, this can be expressed as a convolution:

$$\langle\varphi\rangle_L(\boldsymbol{x}) = \int_{\Omega_\mathrm{f}(z)} \mathcal{A}(\boldsymbol{x}_h - \boldsymbol{y}_h)\varphi(\boldsymbol{y}_h, z)\,\mathrm{d}\boldsymbol{y}_h, \qquad (1)$$

where $\boldsymbol{x} = [\boldsymbol{x}_h; z]$, with $\boldsymbol{x}_h = [x, y]^\mathrm{T}$ representing the streamwise and spanwise directions and z the vertical coordinate. The filter $\mathcal{A}(\boldsymbol{x}_\mathrm{h})$ is square and symmetric, centred at $\boldsymbol{x}_\mathrm{h}$. The filter has value L^{-2} inside the kernel but is 0 elsewhere, ensuring the filter is normalised $\int \mathcal{A}(\boldsymbol{x}_\mathrm{h})\,\mathrm{d}\boldsymbol{x}_\mathrm{h} = 1$. The length L represents the averaging scale: the larger the value of L, the coarser the resulting field $\langle\varphi\rangle_L$. For simplicity, the subscript can be omitted when referring to a general concept if the averaging length L is not emphasised, for example, $\langle\varphi\rangle(\boldsymbol{x})$. In particular, when the averaging length L is much larger than the characteristic urban length-scale ℓ, that is, $L/\ell \gg 1$ or $L = \infty$, the quantity $\langle\varphi\rangle_\infty$ is identical to the conventional superficial plane-average $\langle\varphi\rangle_{xy}$, which is typically defined as (Coceal *et al.*, 2006; Giometto *et al.*, 2016; Nazarian *et al.*, 2020; Sützl *et al.*, 2020; Xie *et al.*, 2008)

1477870x, 0, Downloaded from https://rmets.onlinelibrary.wiley.com/doi/10.1002/qj.70305 by Imperial College London, Wiley Online Library on [25/09/2026]. See the Terms and Conditions (https://onlinelibrary.wiley.com/terms-and-conditions) on Wiley Online Library for rules of use; OA articles are governed by the applicable Creative Commons License

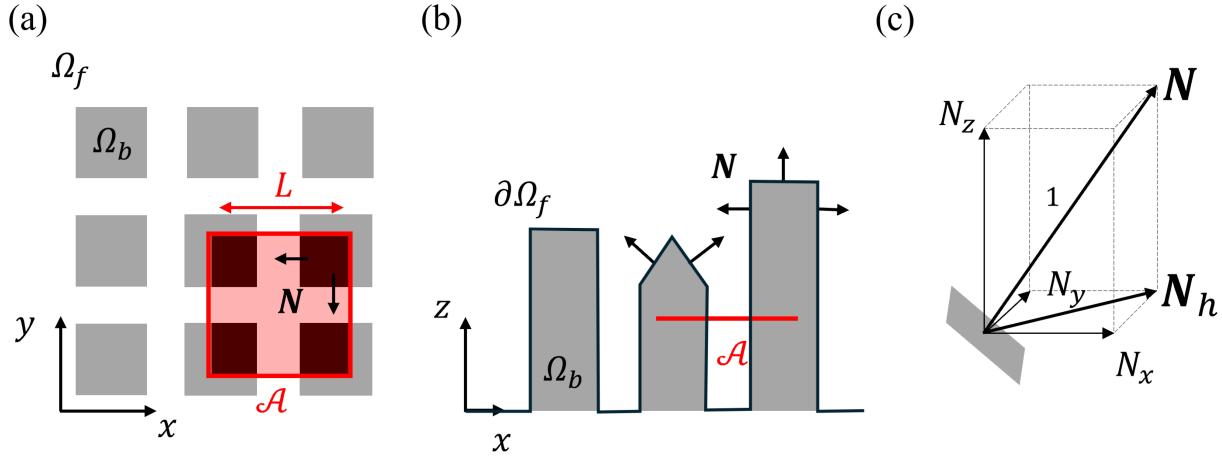


FIGURE 1 Definition sketch of domain and filter $\mathcal{A}$: (a) plan view, (b) elevation view. The domain Ω comprises a fluid subdomain Ω_f (in white), a solid subdomain Ω_b (in grey), and a fluid–solid interface $\partial\Omega_f$ (solid black lines). The building-surface 3-D normal vectors $\boldsymbol{N}$ point into the fluid domain and the decomposition of $\boldsymbol{N}$ is shown in (c). The 2-D square filter $\mathcal{A}$ with averaging length L is shown in red. [Colour figure can be viewed at wileyonlinelibrary.com]

$$\langle\varphi\rangle_{xy}(z) = \frac{1}{A_T}\int_{\Omega_f(z)} \varphi(\boldsymbol{x})\,\mathrm{d}\boldsymbol{x}_h, \tag{2}$$

where A_T is the total area of the horizontal plane.

In the presence of immersed solid boundaries, however, planar averaging and spatial differentiation do not commute. Planar averaging over the differentiation introduces an additional Leibniz-like line integral along the fluid–solid boundary $\partial\Omega_f$ at a given height within the support of the filter $\mathcal{A}$ (Schmid *et al.*, 2019; Van Reeuwijk *et al.*, 2021; Whitaker, 1999). For a scalar field φ and a vector field $\boldsymbol{F}$ with components F_i, it gives

$$\left\langle\frac{\partial\varphi}{\partial x_i}\right\rangle = \frac{\partial\langle\varphi\rangle}{\partial x_i} - \oint_{\partial\Omega_f} \mathcal{A}\varphi\frac{N_i}{|\boldsymbol{N}_h|}\,\mathrm{d}s, \tag{3}$$

$$\left\langle\frac{\partial F_i}{\partial x_i}\right\rangle = \frac{\partial\langle F_i\rangle}{\partial x_i} - \oint_{\partial\Omega_f} \mathcal{A}\frac{F_iN_i}{|\boldsymbol{N}_h|}\,\mathrm{d}s, \tag{4}$$

respectively. Here $\boldsymbol{N} = [N_x, N_y, N_z]^T$ is the three-dimensional surface-normal vector pointing into the fluid domain, as illustrated in Figure 1c, and $\boldsymbol{N}_h = [N_x, N_y]^T$ is its projection onto the horizontal plane.

2.2 | Planar-averaged stresses

In this section, we show the exact form of the equations that need to be solved by non-building-resolving NWP models in order to represent the effect of buildings. For simplicity, we restrict ourselves to a neutral case in which the x-direction is aligned with the mean wind, driven with a large-scale forcing $f(\boldsymbol{x})$. The Reynolds (time)-averaged velocity and kinematic pressure are denoted by $\overline{u}_i$ and $\overline{p}$, respectively, with $\overline{u}$ representing the streamwise (x) velocity component. Thus, the steady Reynolds-averaged streamwise horizontal momentum equation can be written as

$$\frac{\partial\overline{u}_j\overline{u}}{\partial x_j} + \frac{\partial\overline{u_j'u'}}{\partial x_j} + \frac{\partial\overline{p}}{\partial x} = f + \nu\frac{\partial^2\overline{u}}{\partial x_j^2}. \tag{5}$$

Applying the spatial averaging theorem (Equations 1, 3, and 4), this equation becomes (van Reeuwijk & Huang, 2025b)

$$\frac{\partial\langle\overline{u}_i\rangle\langle\overline{u}\rangle}{\partial x_i} + \frac{\partial\langle\overline{p}\rangle}{\partial x} = \langle f\rangle - \langle f_D\rangle + \frac{\partial\langle\tau_i\rangle}{\partial x_i}, \tag{6}$$

where

$$\langle f_D\rangle(\boldsymbol{x}) \equiv \underbrace{-\oint_{\partial\Omega_f} \mathcal{A}\overline{p}\frac{N_x}{|\boldsymbol{N}_h|}\mathrm{d}s}_{\langle f_{D,p}\rangle} + \underbrace{\oint_{\partial\Omega_f} \mathcal{A}\nu\frac{\partial\overline{u}}{\partial x_j}\frac{N_j}{|\boldsymbol{N}_h|}\,\mathrm{d}s}_{\langle f_{D,s}\rangle} \tag{7}$$

is the distributed drag term, comprising a form drag $\langle f_{D,p}\rangle$ associated with pressure and a skin drag $\langle f_{D,s}\rangle$ component associated with viscosity. Note that the velocity vanishes at the building surface $\partial\Omega_f$ owing to the boundary condition. Consequently, after applying Equations (3) and (4), only the boundary-line integrals involving pressure and velocity gradients remain; both are included in the drag term. This equation also indicates that the drag vanishes above the canopy because no fluid–solid interfaces $\partial\Omega_f$ are present there.

The total subfilter stress in Equation (6) is given by

$$\langle\tau_i\rangle(\boldsymbol{x}) \equiv \langle\overline{u}_i\rangle\langle\overline{u}\rangle - \langle\overline{u}_i\overline{u}\rangle - \left\langle\overline{u_i'u'}\right\rangle. \tag{8}$$

1477870x, 0, Downloaded from https://rmets.onlinelibrary.wiley.com/doi/10.1002/qj.70305 by Imperial College London, Wiley Online Library on [25/09/2026]. See the Terms and Conditions (https://onlinelibrary.wiley.com/terms-and-conditions) on Wiley Online Library for rules of use; OA articles are governed by the applicable Creative Commons License

Both the distributed drag (Equation 7) and the subfilter stress (Equation 8) are terms that need to be parameterised in NWP models in order to represent the urban canopy effect on the mean flow. Note that both $\langle f_D \rangle$ and $\langle \tau_i \rangle$ terms are functions that depend on position $\boldsymbol{x}$ and averaging length L.

It is useful to express the volumetric forcing and drag as the cumulative stresses from height z upwards to the domain top h:

$$\tau_{f;L}(\boldsymbol{x}_h, z) \equiv \int_z^h \langle f \rangle_L(\boldsymbol{x}_h, z')\, \mathrm{d}z', \tag{9}$$

$$\tau_{D;L}(\boldsymbol{x}_h, z) \equiv \int_z^h \langle f_D \rangle_L(\boldsymbol{x}_h, z')\, \mathrm{d}z' \,. \tag{10}$$

A main conclusion in van Reeuwijk and Huang (2025b) states how the momentum balance equation (Equation 6) can be simplified under multiple resolutions: in the conventional horizontal plane-averaged sense, it is homogeneous in x and y directions, that is, the averaging length is significantly large, $L = \infty$, that the horizontal components in Equation (6) vanish; when rewriting the equation by integrating it over height, we obtain the following balance:

$$\langle \tau_z \rangle_\infty(z) = \tau_{f;\infty}(z) - \tau_{D;\infty}(z), \tag{11}$$

which illustrates that the vertical transport of the streamwise velocity $\langle \tau_z \rangle_\infty$ is balanced by the imposed large-scale forcing and the building-induced drag. At the ground surface, $z = 0$, Equation (11) reduces to $\tau_{f;\infty}(0) = \tau_{D;\infty}(0) \equiv \tau_0$, where τ_0 is the kinematic surface shear stress (Pope, 2000).

Under periodic boundary conditions, application of the triple decomposition gives (Finnigan, 2000; Nepf, 2012; Raupach & Shaw, 1982)

$$\langle \tau_z \rangle_\infty = -\langle \overline{w}\, \overline{u} \rangle_\infty - \left\langle \overline{w'u'} \right\rangle_\infty = -\langle \overline{w}''\overline{u}'' \rangle_\infty - \left\langle \overline{w'u'} \right\rangle_\infty, \tag{12}$$

where $\langle \overline{w}''\overline{u}'' \rangle_\infty(z)$ is the dispersive stress term, representing the covariance of spatial deviations from the plane-averaged velocities.

2.3 | Parameterisations of drag and kinematic stress

Neither the drag nor the kinematic stress is resolved in NWP models; both therefore require parameterisations (Pope, 2000; Raupach & Shaw, 1982). van Reeuwijk and Huang (2025b) proposed local parameterisations:

$$\frac{\tau_{D;L}}{\tau_{0;L}} = A\zeta_L^3 - B\zeta_L^2 + (1 - A - B)\zeta_L, \tag{13}$$

$$\frac{\langle \tau_z \rangle_L}{\tau_{0;L}} = 1 - A\zeta_L^3 + B\zeta_L^2 - (1 - A - B)\zeta_L, \tag{14}$$

where $\langle \tau_z \rangle_L$ is the vertical kinematic stress within the filter. The parameterisations only depend on the initial conditions and morphology layout, represented by the cumulative normalised frontal area of the buildings over the horizontal plane $\zeta(z)$, with coefficients A and B.

$$\zeta(z) = A_F^{-1} \int_z^{h_{max}} L_b(z')\, \mathrm{d}z', \qquad A_F = \int_0^{h_{max}} L_b(z')\, \mathrm{d}z', \tag{15}$$

where L_b is the frontal building width, A_F the frontal building area, and h_{max} represents the maximum building height. Correspondingly, $\zeta_L(\boldsymbol{x})$ is the frontal-area index covered by the filter, and it becomes ζ at $L = \infty$. We define the planar-averaged surface shear stress $\tau_{0;L} \equiv \tau_{D;L}(z = 0)$. Sützl *et al.* (2020) identified the parameterisation constants $A = 1.88$ and $B = 3.89$ for $\lambda_p = 0.45$, $\lambda_f = 0.22$, but also noted that they are dependent on the morphological configuration. This morphology dependence is consistent with broader evidence that closure parameters in urban canopy models are not universal: Blunn *et al.* (2022), for instance, reported that the von Kármán coefficient varies by roughly a factor of 2.5 across idealised cube and cuboid arrays alone, with no clear systematic relationship to packing density.

It is important to note that the parameterisations in Equations (13) and (14) were originally concluded from the plane-average balance, Equation (11); therefore, they remain most accurate at large enough L that a horizontal homogeneity assumption can be made, that is, $L \geq \ell$, but deteriorate as resolution increases, due to the assumption breaking down and the horizontal transport effects becoming significant. Moreover, the turbulence parameterisation, Equation (14) additionally applies a constant-stress canopy-layer assumption (van Reeuwijk & Huang, 2025b), which limits its fidelity further as the resolution increases.

For consistency with earlier studies, we use the conventional notation $\langle \varphi \rangle_{xy}$ instead of $\langle \varphi \rangle_\infty$ and omit the infinity symbol for plane-averaged quantities when $L = \infty$, for example, $\tau_{f;\infty} \equiv \tau_f$, $\tau_{D;\infty} \equiv \tau_D$. Table 1 summarises the variables and symbols introduced in this section. The details of calculating $\langle f_D \rangle$ and ζ_L within an arbitrary filter require conversion of facet data into the Cartesian field, which is summarised in the Appendix.

3 | SIMULATION DETAILS

Figure 2 presents the urban morphology used in the simulations. The reference site is the campus of the University

1477870x, 0, Downloaded from https://rmets.onlinelibrary.wiley.com/doi/10.1002/qj.70305 by Imperial College London, Wiley Online Library on [25/09/2026]. See the Terms and Conditions (https://onlinelibrary.wiley.com/terms-and-conditions) on Wiley Online Library for rules of use; OA articles are governed by the applicable Creative Commons License

TABLE 1 List of variables and symbols used in the following multi-scale analysis. The third column gives the abbreviated notation used when L need not be specified, and the fourth gives the notation for $L = \infty$.

Name	Variable	Short notation	$L = \infty$
Planar-averaged drag with averaging length L	$\langle f_D \rangle_L(\boldsymbol{x})$	$\langle f_D \rangle$	$\langle f_D \rangle_{xy}(z)$
Planar-averaged volumetric forcing with averaging length L	$\langle f \rangle_L(\boldsymbol{x})$	$\langle f \rangle$	$\langle f \rangle_{xy}(z)$
Planar-averaged stress with averaging length L	$\langle \tau_z \rangle_L(\boldsymbol{x})$	$\langle \tau_z \rangle$	$\langle \tau_z \rangle_{xy}(z)$
Vertical integral of $\langle f_D \rangle_L$	$\tau_{D;L}(\boldsymbol{x})$		$\tau_D(z)$
Vertical integral of $\langle f \rangle_L$	$\tau_{f;L}(\boldsymbol{x})$		$\tau_f(z)$
Kinematic surface shear stress with averaging length L	$\tau_{0;L}(\boldsymbol{x}_h)$		$\tau_0 \equiv \tau_D(0) = \tau_f(0)$

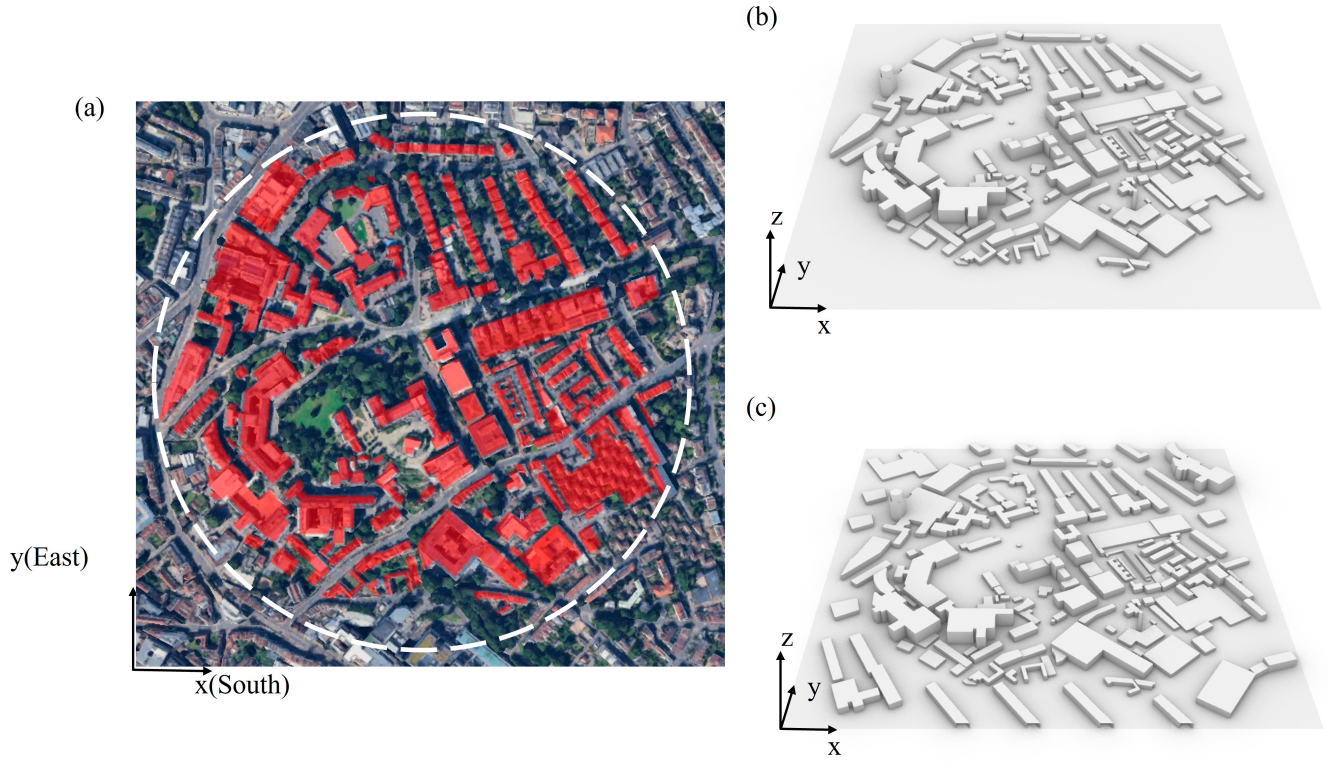


FIGURE 2 (a) Satellite image of the Bristol campus, with the building footprints overlaid; the dashed circle highlights the circular building configuration occupying the central area. (b) The morphology of the "circular" case (CC) extracted directly from the map. (c) The morphology of the "square" case (SC), filling the corners in (b) with additional buildings. [Colour figure can be viewed at wileyonlinelibrary.com]

of Bristol (Figure 2a), one of the focus sites of the ASSURE project. Although the campus buildings naturally cluster around the main quadrangle, the precise circular footprint of the simulation domain is not a feature of the campus itself but is inherited from the corresponding wind-tunnel model deployed at EnFlo (Bi *et al.*, 2025). In wind-tunnel practice, an urban patch is constructed as a disc mounted on a turntable, so that the incoming wind direction can be varied freely without re-machining the model; the disc therefore defines the buildable region of the experiment. The present LES geometry adopts the same disc cutout from the campus at 1:1 scale (Figure 2b). When this disc is placed inside the square periodic computational patch ($L_x \times L_y \times L_z = 800\ \text{m} \times 800\ \text{m} \times 300\ \text{m}$), the four corners of the patch—together about one quarter of A_T—remain as open space surrounding the buildings. We hereafter refer to this geometry as the *disc configuration* of the campus, denoted "circular case" (CC). Beyond its experimental provenance, the disc configuration is well-suited to the present multi-scale analysis: the contrast between the densely built disc and the surrounding open corners generates morphological heterogeneity at the neighbourhood scale, complementing the building-scale variability inherent to any realistic urban morphology.

1477870x, 0, Downloaded from https://rmets.onlinelibrary.wiley.com/doi/10.1002/qj.70305 by Imperial College London, Wiley Online Library on [25/09/2026]. See the Terms and Conditions (https://onlinelibrary.wiley.com/terms-and-conditions) on Wiley Online Library for rules of use; OA articles are governed by the applicable Creative Commons License

The buildings within the disc exhibit diverse shapes and orientations, with a mean building height of $h_m = 12\,m$. The tallest building is a tower in the northeast, reaching $h_{max} = 63\,m$. The plan-area index and frontal-area index are $\lambda_p \equiv A_p/A_T = 0.24$ and $\lambda_f \equiv A_F/A_T = 0.12$, respectively, where A_p is the total building plan area, A_F the frontal area, and $A_T = L_x L_y$ the horizontal domain area. These values reflect a layout with relatively extensive horizontal coverage (wide rooftops) but limited vertical development.

The simulations are performed under periodic boundary conditions, and two morphological configurations are considered (Figure 2b,c). The first is the disc configuration described above, hereafter CC. The second is a numerical modification, the "square" case (SC), in which the four open corners surrounding the disc are infilled with additional buildings sampled from the campus. This raises the plan-area index from $\lambda_p = 0.24$ to 0.31 and the frontal-area index from $\lambda_f = 0.12$ to 0.15, while leaving the mean building height essentially unchanged. SC has no wind-tunnel counterpart; it is constructed numerically to suppress the neighbourhood-scale morphological heterogeneity introduced by the open corners, leaving variability primarily at the building scale. Together, the two simulations enable a direct comparison between layouts governed by different scales of morphological heterogeneity.

The simulations of urban flow over both morphologies were carried out using LES with the open-source code uDALES (Owens *et al.*, 2024; Suter *et al.*, 2022), which is a well-established LES code that has demonstrated excellent performance in numerous previous studies, including comparisons against wind-tunnel experiments (Fellini *et al.*, 2026; Lim *et al.*, 2022; Owens *et al.*, 2024). Solid boundaries were represented by the immersed boundary method (IBM: Suter *et al.*, 2022; Uno *et al.*, 1995). All solid surfaces were treated as aerodynamically rough, with the wall shear stress parameterised using a logarithmic wall model with a prescribed roughness length. We note that the wall model cannot capture local non-equilibrium effects associated with flow separation, reattachment, and rapidly varying pressure gradients fully. However, their impact on the quantities examined in this study is expected to be minor, as we focus mainly on canopy-scale flow statistics rather than local wall dynamics. In particular, the LES resolved the pressure field directly and thus the associated form drag, which dominates over skin drag at wall surfaces.

The turbulent eddy viscosity is calculated using the Vreman (2004) subgrid-scale (SGS) model. The Vreman model is an eddy-viscosity closure in which the subgrid-scale viscosity is computed from the resolved velocity-gradient tensor and the local filter widths. Unlike the classical Smagorinsky model (Smagorinsky, 1963), the Vreman model automatically yields zero subgrid-scale viscosity in several flow configurations that require no subgrid-scale dissipation. The model has demonstrated robust performance in strongly sheared and wall-bounded turbulent flows, while remaining comparable computationally with the Smagorinsky model. These properties make it well-suited to urban-canopy LES involving complex, building-induced turbulence.

The code employs a second-order central-difference scheme on a staggered Arakawa C-grid for spatial discretisation and an explicit third-order Runge–Kutta scheme for time integration.

For both cases, the simulation domain size is $L_x \times L_y \times L_z = 800\,m \times 800\,m \times 300\,m$ with a grid resolution of $N_x \times N_y \times N_z = 400 \times 400 \times 300$, corresponding to cell sizes of $\Delta x \times \Delta y \times \Delta z = 2\,m \times 2\,m \times 1\,m$. Following Xie and Castro (2006), a horizontal resolution of approximately 1/16 of the mean building width is sufficient to predict drag and turbulence statistics in urban-canopy LES. The present resolution is approximately 1/30 of the mean building width and is therefore substantially finer than the recommended value. Periodic boundary conditions are applied on the lateral boundaries, while at the domain top a no-penetration condition, $w = 0$, is imposed on the normal velocity component and the free-slip conditions

$$\frac{\partial u}{\partial z} = \frac{\partial v}{\partial z} = 0$$

are imposed on the tangential velocity components. Atmospheric stability is neutral, with the wind driven by a constant streamwise body force $-\mathrm{d}P/\mathrm{d}x = 1.25 \times 10^{-5}\,kg{\cdot}s^{-2}\,{\cdot}m^{-2}$ in the streamwise (x) direction. Each simulation is run for 72 000 s, corresponding to approximately $450T$; here $T = h_m/u_\tau$ is the canopy eddy-turnover time and u_τ is the friction velocity, which will be introduced later. The final 60 000 s (approximately $375T$) are used to compute time-averaged statistics. To assess statistical convergence, this period is divided into three equal blocks of 20 000 s. The mean velocity, drag, and turbulence statistics obtained from the three blocks show close agreement, indicating that the averaging period is sufficiently long to achieve statistical convergence. The time step is adjusted adaptively based on a maximum CFL number of 1, yielding an average value of approximately 0.65 s ($0.0033T$).

For the multi-scale analysis, eight different horizontal filter lengths were applied: $L = 4, 8, 16, 32, 64, 128, 256$, and 512 m. In addition, the conventional full-plane average over the entire horizontal domain ($800 \times 800\,m^2$) was also included for comparison.

1477870x, 0, Downloaded from https://rmets.onlinelibrary.wiley.com/doi/10.1002/qj.70305 by Imperial College London, Wiley Online Library on [25/09/2026]. See the Terms and Conditions (https://onlinelibrary.wiley.com/terms-and-conditions) on Wiley Online Library for rules of use; OA articles are governed by the applicable Creative Commons License

4 | RESULTS

4.1 | Plane-averaged statistics

We first examine the conventional plane-averaged statistics obtained from the simulations. Figure 3 presents the vertical profiles of the streamwise velocity and kinematic stresses for both cases. The profiles are normalised by the friction velocity $u_\tau = \sqrt{\tau_0}$, where τ_0 is the total surface kinematic stress. This stress can be determined from the imposed forcing via

$$\tau_0 = -\frac{\mathrm{d}P}{\mathrm{d}x}\frac{V_{\mathrm{air}}}{A_{\mathrm{T}}},$$

where V_{air} is the air volume inside the domain. Note that the values of τ_0 and u_τ in both cases coincide, as the difference in V_{air} between the two layouts is negligible.

As shown in Figure 3a, CC has a higher velocity due to fewer building obstacles. Well above the canopy region, that is, for $z \geq 2h_{\max}$, both velocity profiles fit the logarithmic law:

$$\langle \overline{u} \rangle_{xy}(z) = \frac{u_\tau}{\kappa} \ln\left(\frac{z - z_{\mathrm{d}}}{z_0}\right), \tag{16}$$

where $\kappa = 0.41$ is the von Kármán constant, z_{d} is the displacement height, and z_0 is the effective aerodynamic roughness length. The best-fitting parameters are $z_{\mathrm{d}} = 11.10$ m, $z_0 = 1.08$ m for CC and $z_{\mathrm{d}} = 16.00$ m, $z_0 = 1.64$ m for SC. The increase in both displacement and roughness length in SC indicates that the additional buildings elevate the effective level of the mean flow and enhance surface roughness and drag.

Figure 3b shows the vertical profiles of plane-averaged turbulent shear stress $\langle \overline{w'u'} \rangle_{xy}$ and dispersive stress $\langle \overline{w}''\overline{u}'' \rangle_{xy}$. The dispersive stress $\langle \overline{w}''\overline{u}'' \rangle_{xy}$ is significant within the canopy region, indicating strong flow heterogeneity in the mean flow induced by buildings. Above the canopy region, within the roughness sublayer, it decays gradually to zero (e.g., $z > 15h_{\mathrm{m}}$), indicating the transition to the inertial sublayer, where the canopy influence greatly disappears. This also supports the suggestion that the averaging time interval is sufficiently long to ensure statistical convergence. As expected, SC exhibits stronger dispersive stress within the canopy region than CC, due to the additional corner buildings that enhance variability.

Well above the canopy region, Figure 3b shows that the stress $\langle \overline{w'u'} \rangle_{xy}$ for both cases decreases linearly to zero with height, consistent with classical boundary-layer theory. Their decreasing gradients are nearly identical, consistent with the fact that both cases are driven by the same pressure forcing. Interestingly, however, within the canopy region the behaviour departs from previous studies of idealised cube arrays (Coceal & Belcher, 2004; Sützl *et al.*, 2020; van Reeuwijk & Huang, 2025b; Xie *et al.*, 2008), where $\langle \overline{w'u'} \rangle_{xy}$ typically increases monotonically from the ground to the canopy top. In the current realistic cases, $\langle \overline{w'u'} \rangle_{xy}$ first increases to a peak at approximately half the canopy height, but then decreases slightly before reaching the canopy top. This is because of this specific campus morphology: above half the canopy height, only the tall tower and a few isolated buildings remain and the drag decreases sharply. Consequently,

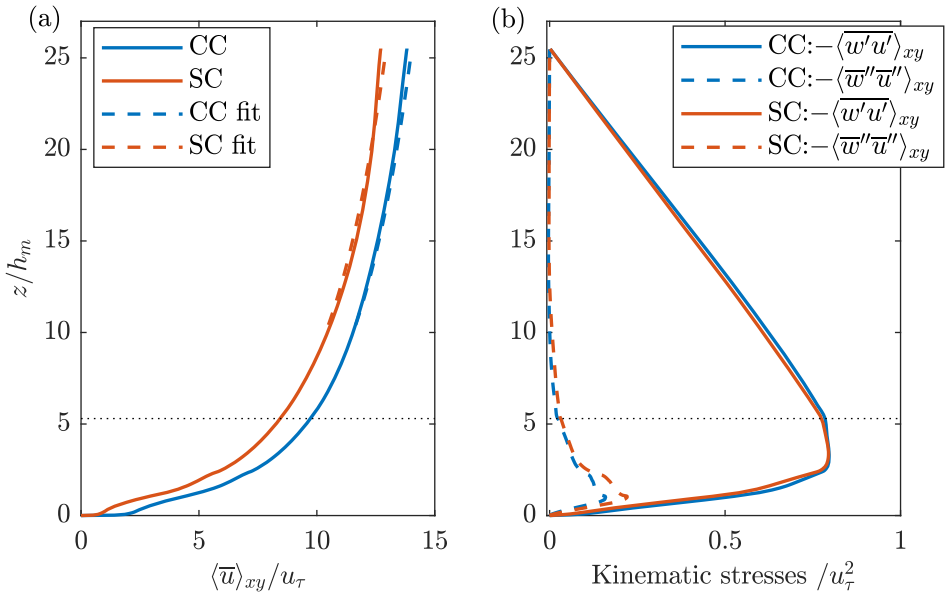


FIGURE 3 Superficial plane-averaged statistics for CC and SC: (a) streamwise velocity with fitted logarithmic profiles and (b) turbulent shear and dispersive stresses. Height is normalised by the mean building height h_{m}, and the horizontal dashed line marks the maximum building height, that is, the canopy top limit. [Colour figure can be viewed at wileyonlinelibrary.com]

1477870x, 0, Downloaded from https://rmets.onlinelibrary.wiley.com/doi/10.1002/qj.70305 by Imperial College London, Wiley Online Library on [25/09/2026]. See the Terms and Conditions (https://onlinelibrary.wiley.com/terms-and-conditions) on Wiley Online Library for rules of use; OA articles are governed by the applicable Creative Commons License

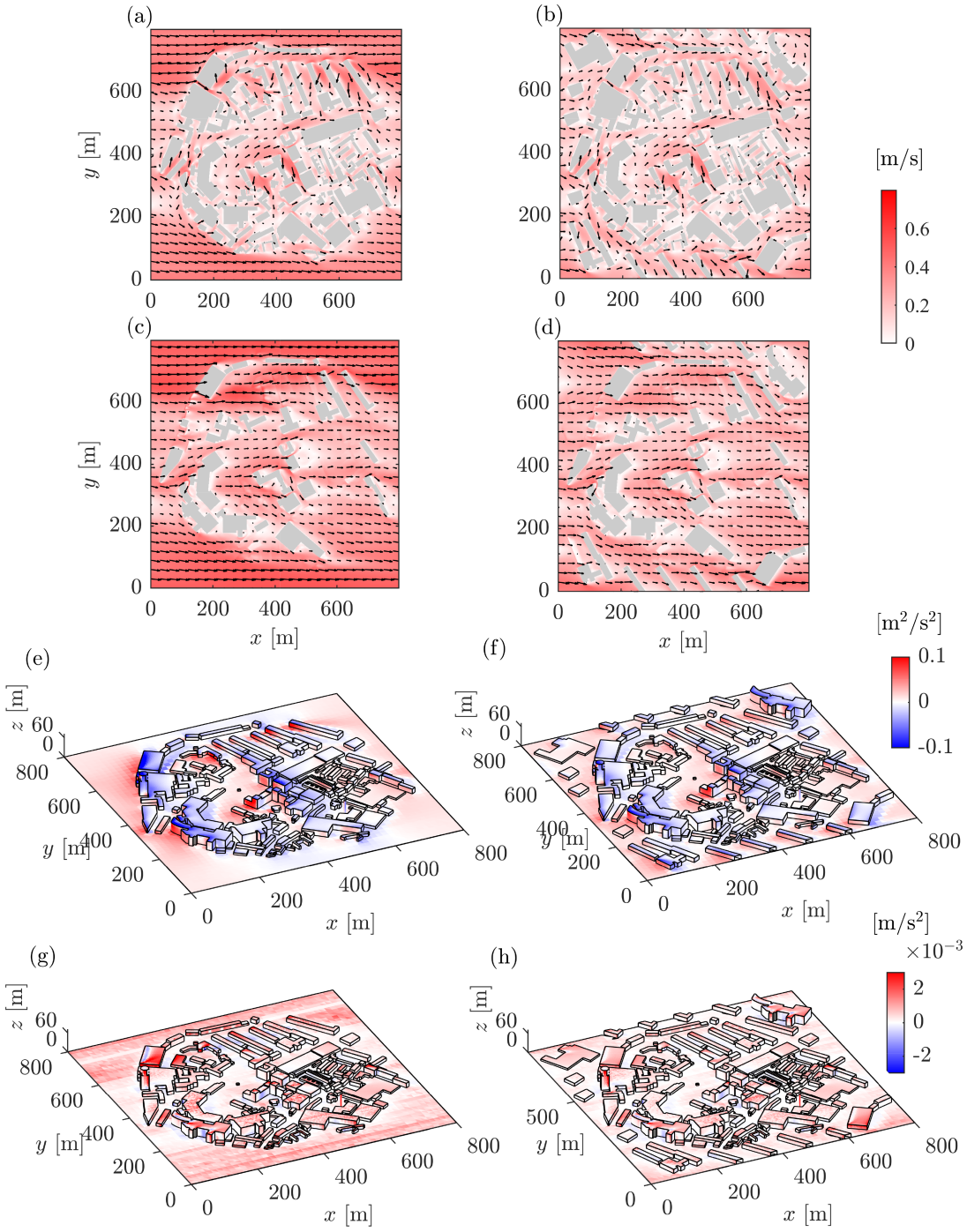


FIGURE 4 The plane view of the time-averaged wind speed (u, v) overlaid with the velocity vectors (a,b) at the pedestrian level ($z = 1.5$ m) and (c,d) at the mean building height ($z = h_m$). The grey area represents the buildings where there is no fluid. (e,f) The surface pressure of the solid phase. (g,h) The surface shear stress is induced by the streamwise velocity. The left column presents the CC, while the right column presents the SC. [Colour figure can be viewed at wileyonlinelibrary.com]

the total kinematic stress $\langle \tau_z \rangle_{xy}$ peaks there, and its main component $\left\langle \overline{w'u'} \right\rangle_{xy}$ also shows a corresponding peak here.

Figure 4 presents a comparison of both cases, with the left column corresponding to CC and the right to SC. The top two rows show the mean wind-speed field, defined as $\sqrt{\overline{u}^2 + \overline{v}^2}$, at pedestrian level $z = 1.5$ m (Figure 4a,b) and at the mean building height $z = h_m = 12$ m (Figure 4c,d), respectively. In Figure 4a, high-speed channelled flow can be observed at the top and bottom sides of the figure, reflecting the absence of building obstacles. This channelled flow is disrupted in the SC case (Figure 4b,d). Near

1477870x, 0, Downloaded from https://rmets.onlinelibrary.wiley.com/doi/10.1002/qj.70305 by Imperial College London, Wiley Online Library on [25/09/2026]. See the Terms and Conditions (https://onlinelibrary.wiley.com/terms-and-conditions) on Wiley Online Library for rules of use; OA articles are governed by the applicable Creative Commons License

the circular building region (grey blocks), the velocity field becomes strongly heterogeneous, with clearly reduced wind speeds. At higher elevation ($z = h_m$), the building area decreases and consequently the flow becomes more homogeneous, as shown in Figure 4c. At this height, the wind direction remains largely aligned with the imposed streamwise forcing and is only deflected locally near buildings.

Figure 4e,f shows the time-averaged building surface pressure field $\overline{p}$, obtained at the nearest grid cells from the building walls. Along the wind direction, the positive x-axis, positive pressure (dark red) occurs on the most windward (frontal) building faces, while negative pressure occurs on the leeward (rear) sides and in wakes. It is this pressure gradient that generates the form drag. In addition, negative pressure regions are clearly visible on building roofs, especially on the windward edges, which is consistent with flow boundary-layer separation at the roof leading edges (Atar & Mercan, 2026). A comparison between Figure 4e and f highlights the shielding effect of the additional buildings: for example, along the upwind strip over $x \approx 150$–200 m, the roofs have less negative pressure in SC, as the incoming flow is decelerated by upstream obstacles.

Finally, Figure 4g,h shows the distribution of shear stress, which arises primarily from the ground surface and building roofs. In CC, the shear stress is particularly strong along the ground-level channels, whereas in SC, due to additional building disruption, most shear stress is distributed to the roofs.

Figure 5 shows the drag-related profiles. Figure 5a,b presents the vertical profiles of the plane-averaged drag force and its form and skin components for CC and SC, respectively. The total drag force, $\langle f_D \rangle_{xy}$, is obtained in two ways: first from the momentum budget closure (Equation 6 with horizontal terms neglected after full-plane averaging) and second from the direct line integral (Equation 7). The results indicate that, in both cases, the two methods are in close agreement: the drag force peaks near the mean building height and diminishes to nearly zero above $z/h_{max} > 0.5$ because little building frontal area remains above this height. This is consistent with building normalised frontal area ζ in Figure 5f, which shows that there is very little building surface area above $z/h_{max} > 0.5$. As suggested by the kinematic stresses in Figure 3b, the overall magnitude of plane-averaged $\langle f_D \rangle_{xy}$ is similar between the two cases, with SC slightly larger. However, the skin drag at the ground level $z = 0$ in CC is significantly greater than in SC. This agrees with the ground shear stress distributions shown in Figure 4g,h and is confirmed quantitatively here.

Although the form drag $\langle f_{D,p} \rangle_{xy}$ dominates the total drag in both cases and is the primary concern in this study, we acknowledge that surface shear stress (the skin drag) can be locally important at several particular heights. For example, at $z/h_{max} \approx 0.4$, shear stress contributes up to nearly half of the total drag. This can be attributed to the large footprint of the buildings, as indicated by the plan-area index λ_p. Since drag components can only be determined directly from Equation (7), hereafter, we will use Equation (7) to calculate the drag for further analysis.

Figure 5c presents the vertical profiles of the drag coefficient $C_d(z)$ (Coceal & Belcher, 2004; Santiago & Martilli, 2010), which relates directly to the distributed drag $\langle f_D \rangle_{xy}$ through

$$\langle f_D \rangle_{xy} = \frac{1}{2} \frac{L_b}{A_T} C_d \langle \overline{u} \rangle_{xy}^2. \tag{17}$$

It is an alternative form of drag parameterisation to Equation (13), and this drag coefficient C_d is widely adopted in engineering practice; therefore, it is useful to include it here. The drag coefficient is very large near the ground due to the low plane-averaged velocities, which is consistent with Coceal and Belcher (2004). SC exhibits larger C_d values than CC throughout the lower half of the canopy, due to the additional buildings. In the upper half, the difference decreases due to the absence of additional buildings. The drag coefficient obtained here is lower than that reported for idealised staggered arrays (between 2 and 3) by Coceal and Belcher (2004). The building orientation is likely one of the reasons for this discrepancy: in the present cases, varied building alignments deflect flow and reduce streamwise drag, whereas, in the idealised cases of Coceal and Belcher (2004), wind is always perpendicular to the cubes.

Figure 5d,e shows the plane-averaged cumulative stresses, which satisfy the balance in Equation (11). In line with the calculation of τ_0, the surface kinematic stresses are nearly identical for both cases. Recall that $\langle \tau_z \rangle_{xy}$ represents the superposition of turbulent and dispersive stresses (Equation 12), already shown in Figure 3b. This stress peaks near the mean building height and decreases linearly above the canopy. The cumulative drag τ_D decreases smoothly with height, but its gradient steepens at approximately $z/h_{max} = 0.5$, coinciding with the sudden reduction in building area, consistent with the vertical profiles in Figure 5a,b,f.

The drag parameterisation (Equation 13) in the plane-averaged sense is examined in Figure 5g,h. This figure illustrates the evolution of τ_D with $1 - \zeta$ (where $1 - \zeta = 0$ corresponds to the ground), overlaid with the parameterisations. Note that the parameterisation in Equation (13) originally considered only the form drag and neglected the skin drag; therefore, both the full cumulative drag τ_D and the form-drag-only component τ_D^p are

1477870x, 0, Downloaded from https://rmets.onlinelibrary.wiley.com/doi/10.1002/qj.70305 by Imperial College London, Wiley Online Library on [25/09/2026]. See the Terms and Conditions (https://onlinelibrary.wiley.com/terms-and-conditions) on Wiley Online Library for rules of use; OA articles are governed by the applicable Creative Commons License

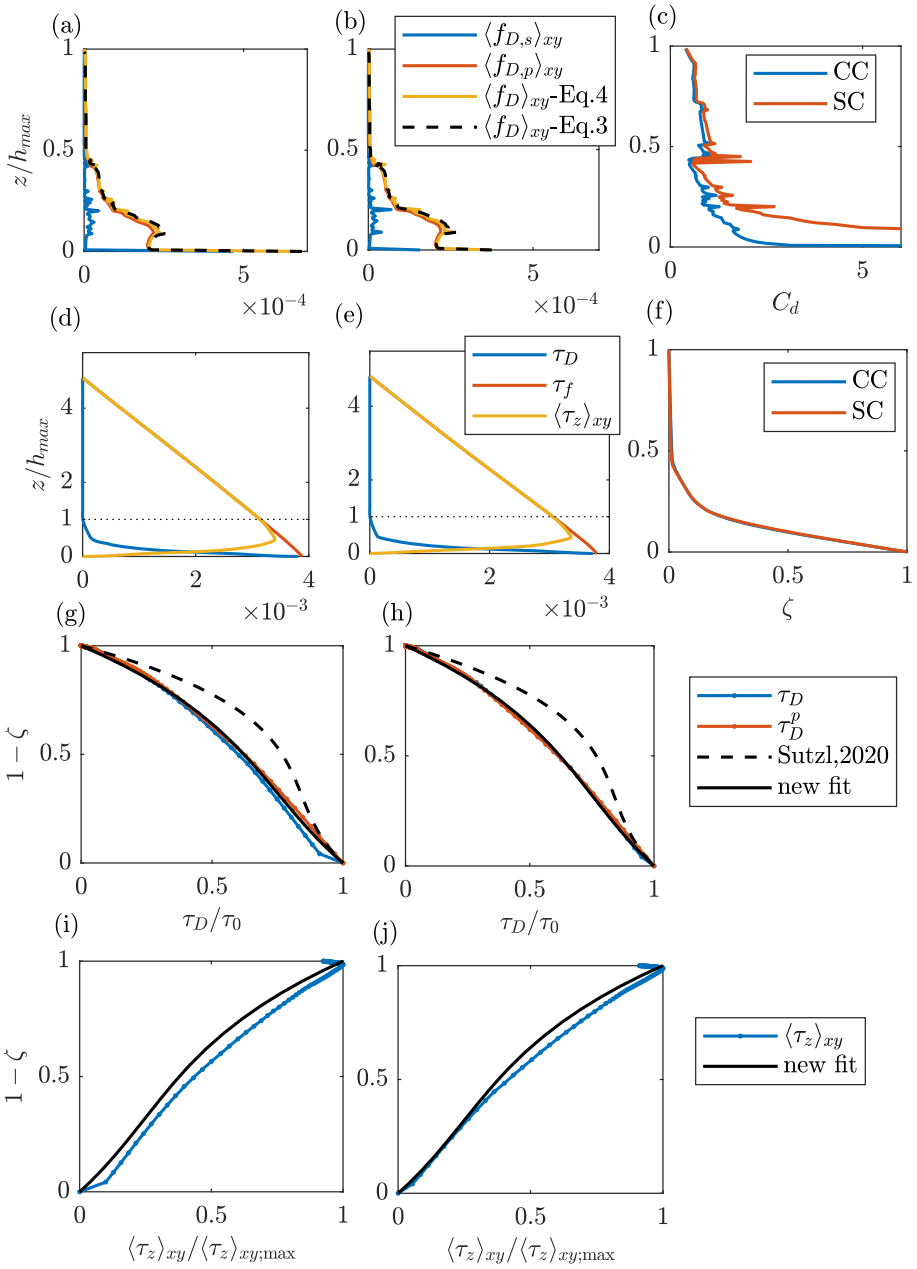


FIGURE 5 The vertical profile of plane-averaged (a,b) drag force and its components (unit m·s^{-2}) and (d,e) cumulative stresses (unit m^2 ·s^{-2}); the height is normalised by the maximum building height, marked as the horizontal dotted lines. (g,h) The cumulative drag stress τ_D against the normalised frontal area ζ, overlaid with the parameterisation Equation (13) at $L = \infty$; (i,j) the cumulative turbulent stress $\langle\tau_z\rangle$ against the normalised frontal area ζ, overlaid with the parameterisation Equation (14) at $L = \infty$. The first column shows the profiles of CC, while the second column shows those of SC. (c) shows the vertical profile of the drag coefficient C_d; (f) shows the vertical profile of normalised frontal area ζ for both cases. [Colour figure can be viewed at wileyonlinelibrary.com]

presented here. Typically, in terms of the vertical accumulation, the skin drag component is indeed negligible, as τ_D and τ_D^p are nearly identical except at $1-\zeta = 0$ in CC, where the large ground shear stress produces a discrete jump. Because this contribution is confined to the ground surface, it does not affect the profiles above the ground. However, neither of the profiles matches the parameterisation of Sützl *et al.* (2020) (dashed lines), which overestimates drag substantially. This discrepancy exists because the parameterisation constants depend on morphological parameters: the constants in Sützl *et al.* (2020), $A = 1.88$, $B = 3.89$, were derived from morphologies with larger plan- and frontal-area indices than in the present study. The mismatch reflects the dependence of the fitted coefficients on morphology, particularly the plan- and frontal-area indices. By refitting Equation (13), new constants $A = 0.89$ and $B = 1.82$ are obtained, shown as solid black lines in Figure 5g,h. The coefficient of determination $R^2 > 0.998$ for both cases indicates good agreement.

Finally, Figure 5i,j evaluates the parameterisation of turbulent stress $\langle\tau_z\rangle_{xy}$ using Equation (14) with the newly fitted constants. The refitted parameterisation demonstrates good agreement in both cases. Here, the normalisation is modified slightly: instead of using the surface stress τ_0, the maximum stress $\langle\tau_z\rangle_{xy;\max}$ is adopted to constrain the parameterisation within the unit interval. This follows the constant stress layer assumption (Schlichting & Gersten, 2017), that is, $\tau_f(z < h_{\max}) \approx \tau_0 \approx \langle\tau_z\rangle_{xy;\max}$, which is

1477870x, 0, Downloaded from https://rmets.onlinelibrary.wiley.com/doi/10.1002/qj.70305 by Imperial College London, Wiley Online Library on [25/09/2026]. See the Terms and Conditions (https://onlinelibrary.wiley.com/terms-and-conditions) on Wiley Online Library for rules of use; OA articles are governed by the applicable Creative Commons License

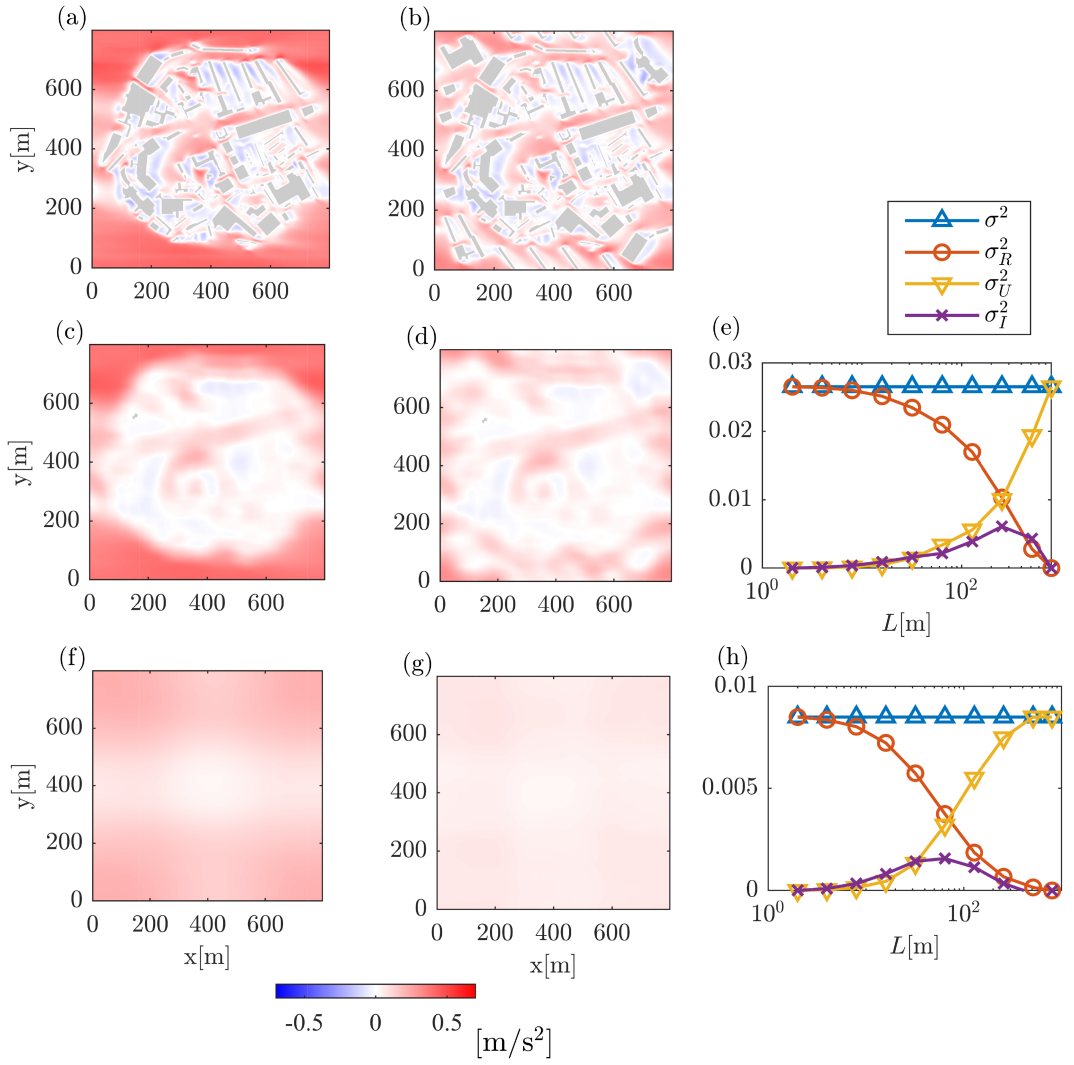


FIGURE 6 The filtered streamwise velocity field $\langle \overline{u} \rangle_L$ at various averaging lengths at the pedestrian level $z = 1.5$ m for (first column) CC and (second column) SC: averaging lengths (a,b) $L = 8$ m, (c,d) $L = 64$ m, and (f,g) $L = 512$ m; (e,h) are the variances of the streamwise velocity at pedestrian level for CC and SC, respectively. [Colour figure can be viewed at wileyonlinelibrary.com]

more accurate when the domain height is much greater than the canopy height. The normalised stress decreases monotonically with $1 - \zeta$, except near $1 - \zeta = 1$ (the upper half of the canopy), where minor deviations occur but remain close to the fitted curve.

Overall, the revised parameterisation (Equation 14) with the new constants represents the plane-averaged kinematic stress within the canopy for the present morphologies reasonably well.

4.2 | Multi-scale analysis of flow heterogeneity

We next apply the framework, demonstrated previously for idealised geometries (van Reeuwijk & Huang, 2025b), to realistic campus layouts. The first two columns in Figure 6 show the coarse-grained streamwise velocity $\langle \overline{u} \rangle_L$ at pedestrian level ($z = 1.5$ m) for CC and SC, obtained with averaging lengths $L = 8, 64$, and 512 m. The sequence illustrates clearly how the field evolves with the averaging length-scale. At the relatively short length-scale (corresponding to relatively high resolution) $L = 8$ m (Figure 6a,b; note that the original resolution of the field is 1 m), the details of the velocity field are retained clearly, showing strong heterogeneity: individual buildings remain visible and negative velocities appear in the wakes and street canyons. At $L = 64$ m (Figure 6c,d), the velocity fields become smoother and only large-scale features can still be identified, such as the long street extending from $x = 200$ m, $y = 400$ m to $x = 700$ m, $y = 500$ m. At this length-scale, the velocity signatures of individual buildings are largely removed and their footprint is represented by very low velocities.

1477870x, 0, Downloaded from https://rmets.onlinelibrary.wiley.com/doi/10.1002/qj.70305 by Imperial College London, Wiley Online Library on [25/09/2026]. See the Terms and Conditions (https://onlinelibrary.wiley.com/terms-and-conditions) on Wiley Online Library for rules of use; OA articles are governed by the applicable Creative Commons License

Interestingly, in CC (Figure 6c), these low-velocity regions trace out the outline of the disc configuration clearly, with the building-occupied cluster standing apart from the higher-velocity open corners. At the largest averaging length-scale $L = 512$ m, corresponding to the lowest resolution (Figure 6f,g), the velocity fields become nearly homogeneous and close to the full plane average. Although no velocity details remain, a difference can still be observed: in CC (Figure 6f), the four corners exhibit higher velocities while the centre shows lower values; however, in SC such a feature is not significant, due to the additional buildings at the corners. It is worth noting that even the coarsest length-scale here, $L = 512$ m, remains finer than the resolution at which urban effects are parameterised in most NWP models.

The spatial heterogeneity of the streamwise velocity $\overline{u}$ is quantified by its variances (van Reeuwijk & Huang, 2025b; Yu *et al.*, 2023). The plane-averaged variance σ^2 is defined as

$$\sigma^2(z) \equiv \left\langle (\overline{u}(\boldsymbol{x}_h, z) - \langle \overline{u} \rangle_{xy})^2 \right\rangle_{xy}, \tag{18}$$

which can be decomposed as

$$\sigma^2 = \sigma_{\mathrm{R}}^2 + \sigma_{\mathrm{U}}^2 + \sigma_{\mathrm{I}}^2, \tag{19}$$

where

$$\sigma_{\mathrm{U}}^2(z) \equiv \left\langle (\overline{u} - \langle \overline{u} \rangle_L)^2 \right\rangle_{xy}, \tag{20}$$

$$\sigma_{\mathrm{R}}^2(z) \equiv \left\langle (\langle \overline{u} \rangle_L - \langle \overline{u} \rangle_{xy})^2 \right\rangle_{xy}, \tag{21}$$

$$\sigma_{\mathrm{I}}^2(z) \equiv 2\left\langle (\overline{u} - \langle \overline{u} \rangle_L)(\langle \overline{u} \rangle_L - \langle \overline{u} \rangle_{xy}) \right\rangle_{xy}. \tag{22}$$

Here, σ_{U}^2 is the unresolved variance, representing the discrepancy between the local value (e.g., $\overline{u}$) and the planar-averaged value (e.g., $\langle \overline{u} \rangle_L$). A large unresolved variance typically indicates a significant difference between the original high-resolution field and the field at length-scale L, suggesting that the field features at scale L are largely unresolved and therefore require modelling. The component σ_{R}^2 is the resolved variance. A small resolved variance typically implies that the planar-averaged value at scale L is close to the average over the entire horizontal plane (e.g., $\langle \overline{u} \rangle_{xy}$), again indicating that the field at length-scale L is very coarse. A large resolved variance suggests that the field is well resolved. The component σ_{I}^2 is (twice) the interaction covariance (van Reeuwijk & Huang, 2025b). Note that, by definition, the total variance σ^2 is independent of the averaging length L, but its components σ_{U}, σ_R, σ_I are dependent of L.

Figure 6e shows the decomposed variances for CC at pedestrian height, varying with the averaging length L. As L increases, the resolved variance σ_{R}^2 decreases while the unresolved variance σ_{U}^2 increases, consistent with the coarse-graining process in Figure 6a,c,f. At small L, that is, high resolutions, most flow variability is retained explicitly and the resolved variance dominates. At large L, that is, low resolutions, most variability lies below the filter scale and the unresolved variance dominates, indicating a greater need for parameterisation. The length-scale at which the resolved and unresolved variances cross indicates a scale where the resolved and unresolved parts are equally important; therefore, we refer to this length-scale as the characteristic urban length-scale ℓ of the morphology-induced flow heterogeneity. This length-scale provides a concept of the extent to which the field may be regarded as homogeneous. For CC, $\ell \approx 256$ m, which is comparable with the radius of the circular patch and corresponds to a neighbourhood length-scale. This scale indicates that the circularly arranged building cluster can be distinguished from the surrounding open space at an averaging length-scale of approximately 256 m. At coarser resolutions, the filtered field appears effectively homogeneous; in contrast, to capture building-scale structures, like buildings and streets, finer resolutions than this scale are required. Equation (19) indicates that the interaction term σ_{I}^2 is only significant when resolved and unresolved variances are both important, and indeed, in the present results, its peak coincides with ℓ.

Figure 6h presents the same analysis for SC. The total variance is smaller ($\sigma^2 = 0.01$) than in CC ($\sigma^2 = 0.03$), reflecting the more homogeneous velocity distribution at the corners. A key difference is that in SC, as L increases, σ_{R}^2 decreases more rapidly (and, equivalently, σ_{U}^2 increases more rapidly) compared with CC; consequently, the curves intersect at a smaller length-scale $\ell \approx 64$ m. This is because, in CC, high velocities $\langle \overline{u} \rangle_L$ persist in the open corners as L increases, causing σ_{R}^2 to decrease and σ_{U}^2 to increase—more slowly than in SC. This length-scale is comparable with a characteristic building scale, indicating that flow heterogeneity in SC typically occurs at the building scale. At coarser resolutions, such variability is not resolved. We note that, in both cases, although ℓ is formally diagnosed from flow variance, it corresponds closely in these neutral cases to the dominant scale of morphological organisation: the cluster radius in CC and the individual-building scale in SC. This correspondence indicates that the underlying morphology controls the diagnosed flow scale, so that ℓ can also be associated with a characteristic length-scale of morphological heterogeneity.

To examine the height dependence of the diagnosed scale, Figure 7 shows the interaction covariance σ_{I}^2 as a function of L and z. In both cases, σ_{I}^2 is small near and above $h_{\max}$, where the direct influence of the

1477870x, 0, Downloaded from https://rmets.onlinelibrary.wiley.com/doi/10.1002/qj.70305 by Imperial College London, Wiley Online Library on [25/09/2026]. See the Terms and Conditions (https://onlinelibrary.wiley.com/terms-and-conditions) on Wiley Online Library for rules of use; OA articles are governed by the applicable Creative Commons License

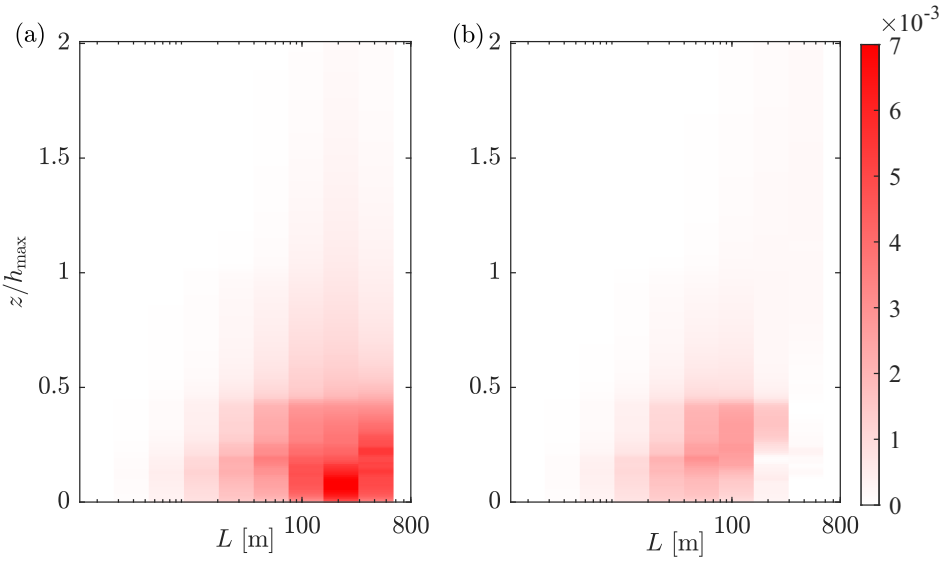


FIGURE 7 Interaction covariances of streamwise velocity as a function of averaging length L and the height z: (a) CC and (b) SC. [Colour figure can be viewed at wileyonlinelibrary.com]

buildings is weak. Within the canopy, it peaks at $L \approx 256$–512 m for CC and $L \approx 64$–128 m for SC, consistent with the pedestrian-level variance crossover. The CC peak is stronger and extends through a greater fraction of the canopy, indicating neighbourhood-scale flow heterogeneity induced by the contrast between the densely built disc and the open corners. In SC, infilling the corners removes this neighbourhood-scale morphological contrast, leaving weaker flow heterogeneity dominated by individual buildings and street canyons. Thus, ℓ depends not only on packing density but also on the spatial organisation of the morphology.

Although the variance analysis above uses the streamwise velocity, the same characteristic length-scale ℓ is recovered when other fields are used: for example, the turbulent kinetic energy field, as demonstrated on idealised geometries by van Reeuwijk and Huang (2025b).

To examine the drag on buildings, Figure 8 presents the spatially averaged kinematic surface stress $\tau_{0;L}$ at three averaging lengths (with length-scale $L = 8, 64, 512$ m). As $\tau_{0;L} \equiv \tau_{D;L}(z = 0)$ (Equation 10), it represents the filter-averaged integral drag force exerted on the buildings. At the smallest averaging length $L = 8$ m (Figure 8a,d), $\tau_{0;L}$ outlines the buildings clearly, as the drag stress mostly occurs at the building surface. A faint red is also visible over the ground, which is due to the ground-surface shear stress. This length-scale provides a detailed view of the stress distribution around individual buildings. For example, in the region $x < 200$ m, the dark red area indicates that the windward-facing buildings experience large drag, while negative drag stress can be observed in the wake region between locally dense building clusters. Note that, as an integral value, the magnitude of $\tau_{0;L}$ is correlated closely with the building height.

At an intermediate length-scale of $L = 64$ m (Figure 8b,e), the drag patterns become more diffuse and individual buildings are no longer visible, consistent with the behaviour seen in Figure 6. Instead, three distinct high-drag regions can be noticed (with dark red): zone A contains the tallest tower, the large height of which enhances drag; zones B and C have relatively high building density and moderate building height, which also generate significant drag. While no strong negative drag areas are apparent at this length-scale, very light blue patches appear downstream of zones B and C, suggesting wake effects in the leeward regions. Thus, at this length-scale, the field suppresses individual-building details while retaining several neighbourhood-scale high-drag regions, which is suitable for monitoring key areas of interest within the domain.

At the largest length-scale $L = 512$ m (Figure 8c,f), spatial heterogeneity in the surface-stress field is no longer clearly visible. The surface stress $\tau_{0;L}$ becomes nearly homogeneous across the entire plane, with magnitudes converging to the global average τ_0.

Since the kinematic surface stress $\tau_{0;L}$ represents the drag acting on buildings and also serves as the normalisation factor in the parameterisation of Equation (13), it is useful to examine how it varies with morphological parameters. Figure 9 shows two joint PDFs of $\tau_{0;L}$ against the local plan-area index $\lambda_{p;L}$ and the frontal-area index $\lambda_{f;L}$ for both cases. Here, we examine $L = 256$ and 512 m, for which horizontal variability is comparatively weak. Recall that this parameterisation is derived from the full-plane momentum balance (Equation 11), in which only vertical transport is considered and horizontal transport is assumed to be negligible.

The broad distribution of $\tau_{0;L}$ across $\lambda_{p;L}$ and $\lambda_{f;L}$ confirms that the constants in the parameterisation

1477870x, 0, Downloaded from https://rmets.onlinelibrary.wiley.com/doi/10.1002/qj.70305 by Imperial College London, Wiley Online Library on [25/09/2026]. See the Terms and Conditions (https://onlinelibrary.wiley.com/terms-and-conditions) on Wiley Online Library for rules of use; OA articles are governed by the applicable Creative Commons License

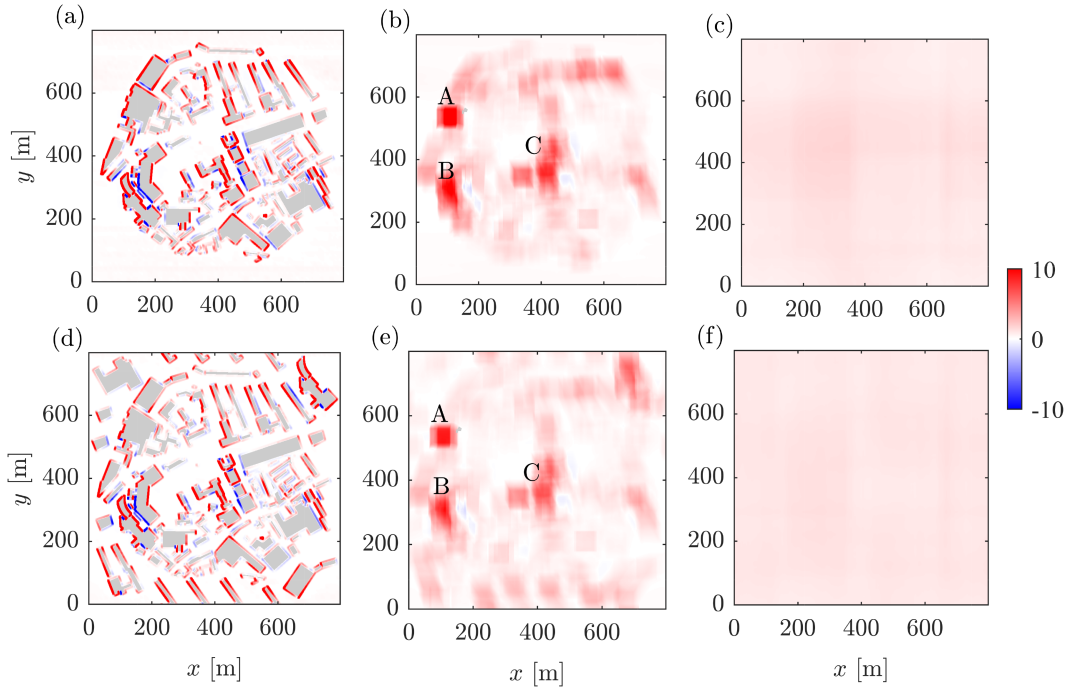
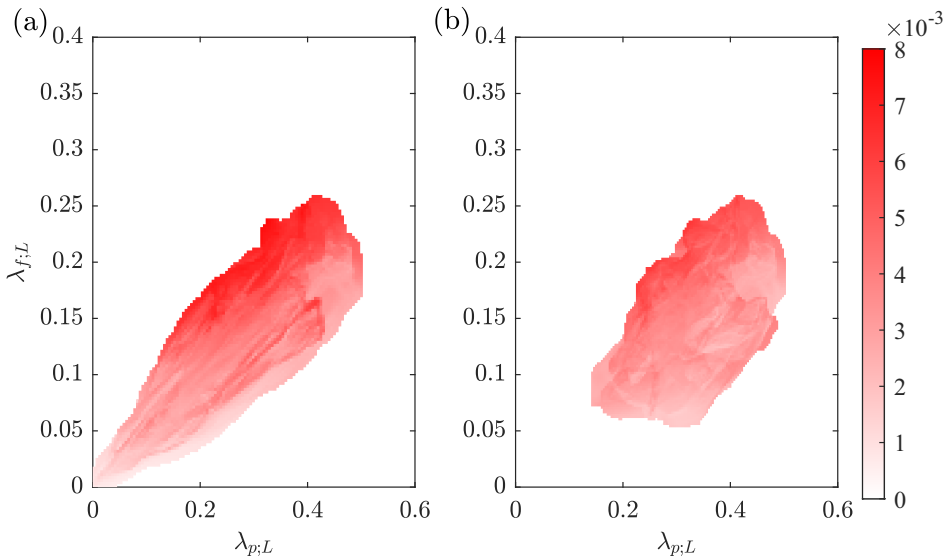


FIGURE 8 The coarse-grained kinematic surface stress $\tau_{0;L}$ for (top row) CC and (bottom row) SC, respectively, with the averaging lengths (a,d) $L = 8$ m, (b,e) $L = 64$ m, and (c,f) $L = 512$ m. Three high-drag zones are labelled in (b,e). [Colour figure can be viewed at wileyonlinelibrary.com]

FIGURE 9 Spatially averaged kinematic surface stress $\tau_{0;L}$ against the plan-area index $\lambda_{p;L}$ and frontal-area index $\lambda_{f;L}$ for (a) CC and (b) SC, respectively. Data at averaging lengths $L = 256, 512$ m are used in both figures. [Colour figure can be viewed at wileyonlinelibrary.com]



(Equation 13) indeed depend on the underlying morphological parameters. The broad ranges of local $\lambda_{p;L}$ and $\lambda_{f;L}$ at the two averaging lengths are consistent with Chen and Dipankar (2022), who reported substantial sub-kilometre variability in urban morphological parameters. As expected, CC (Figure 9a) exhibits a wider spread in both $\lambda_{p;L}$ and $\lambda_{f;L}$ compared with SC (Figure 9b), with an additional "tail" extending toward the origin. This arises because, in CC, the filter can cover corner regions with very few or even no buildings, leading to very low $\lambda_{p;L}$ and $\lambda_{f;L}$ and correspondingly low surface stresses.

An important observation is that, in both morphologies, $\tau_{0;L}$ tends to increase when $\lambda_{f;L}$ increases, as larger building frontal area induces greater drag, or when $\lambda_{p;L}$ decreases, as reduced shielding enhances drag. This trend becomes particularly pronounced for $\lambda_{f;L} > 0.15$. Furthermore, the results indicate that $\tau_{0;L}$ can remain nearly constant if $\lambda_{p;L}$ and $\lambda_{f;L}$ vary simultaneously along a trajectory with an approximate 45° slope, as the opposing effects

1477870x, 0, Downloaded from https://rmets.onlinelibrary.wiley.com/doi/10.1002/qj.70305 by Imperial College London, Wiley Online Library on [25/09/2026]. See the Terms and Conditions (https://onlinelibrary.wiley.com/terms-and-conditions) on Wiley Online Library for rules of use; OA articles are governed by the applicable Creative Commons License

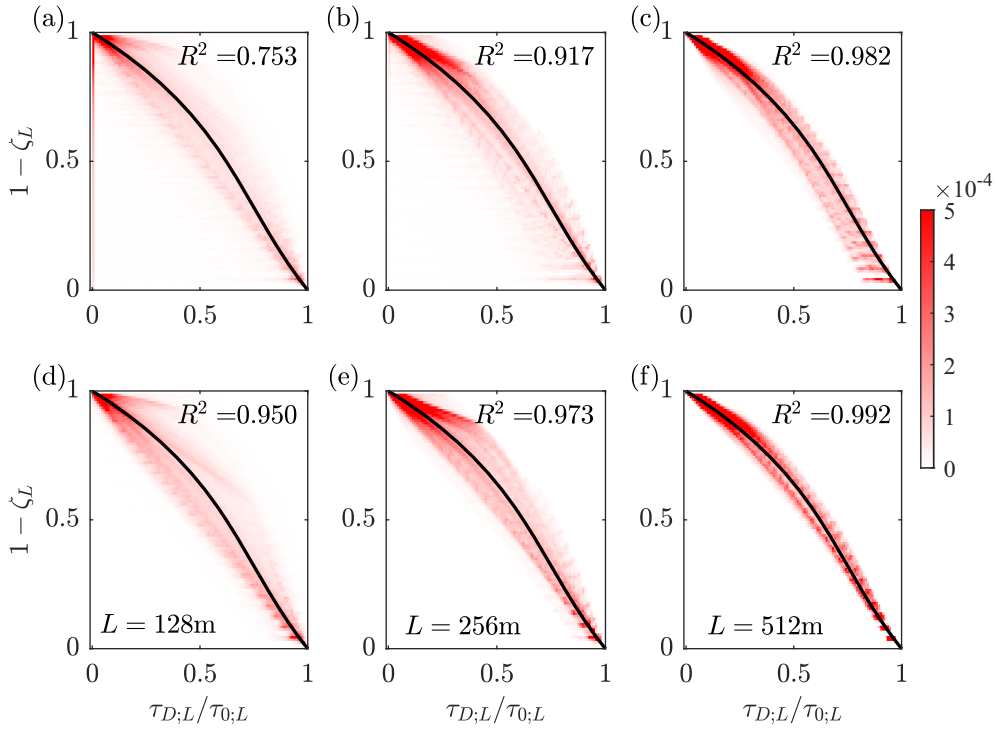


FIGURE 10 The probability density of normalised local cumulative drag stress $\tau_{D;L}/\tau_{0;L}$ against the local scaled frontal area ζ_L at different averaging lengths: (a,d) $L = 128$ m, (b,e) $L = 256$ m, and (c,f) $L = 512$ m, for (top panel) CC and (bottom panel) SC, respectively. Colour indicates the probability density of the samples. The solid line represents the parameterisation Equation (13) with modified constants $A = 0.89$, $B = 1.82$. The coefficient of determination R^2 is labelled to show the performance of the parameterisation. [Colour figure can be viewed at wileyonlinelibrary.com]

of increased frontal area and increased shielding balance each other.

Next, we perform an a priori analysis at different averaging lengths L to evaluate the local drag parameterisation in Equation (13). Figure 10 presents the distribution density of the local cumulative drag stress $\tau_{D;L}$ against the local scaled frontal area ζ_L at three averaging lengths ($L = 128$, 256, and 512 m), overlaid with the parameterisation (with modified constants) for both cases.

The parameterisation performs best for SC at $L = 512$ m (Figure 10f), where $R^2 = 0.998$. At this averaging length, the filtered morphology and drag fields vary only weakly across the domain, and the locally evaluated relationship approaches its full-plane form. As L decreases, more flow heterogeneity and morphological variability are resolved, increasing the scatter around the fitted relation. Horizontal transport terms also become increasingly important, whereas the parameterisation retains only the vertical balance. The parameterisation therefore deteriorates rapidly at $L < 64$ m. Its performance remains reasonable for SC when L is larger than the diagnosed crossover scale.

In contrast, CC shows poorer parameterisation agreement. Even at the same low resolution ($L = 512$ m, Figure 10c), the data distribution exhibits broader scatter around the fitted relation, indicating that the normalised cumulative drag $\tau_{D;L}/\tau_{0;L}$ is hard to converge. This divergence arises because the filter in CC can cover a wider range of morphological conditions, $\lambda_{p;L}$ and $\lambda_{f;L}$, because of the corners (see Figure 9a). Consequently, CC spans a wider range of $\tau_{D;L}$ and $\tau_{0;L}$ than SC. Since coefficients in parameterisation Equation (13) depend on morphology, a single set of constants cannot capture such variability adequately. As a result, the R^2 value in CC (Figure 10c) is significantly lower than that in SC (Figure 10f).

Further decreasing L, Figure 10a,b presents an even worse fit, compared with either Figure 10c in the same case or Figure 10d,e at the same resolution, respectively. Notably, Figure 10a shows instances with $\tau_{D;L}/\tau_{0;L} \approx 0$, corresponding to filters that cover very little building area, thus almost no drag—for example, at open corner regions. Such cases hardly appear at larger L, where filters inevitably include more buildings. For CC, the averaging length at which the parameterisation still performs reasonably is around $L = 256$ m, which aligns with its characteristic length-scale.

Figure 11 presents the performance of the total kinematic stress parameterisation (Equation 14) with the modified constants. Although the parameterisation reproduces the plane-averaged profiles reasonably well (see Figure 5i,j), its accuracy declines as L decreases. Only at the coarsest resolution (largest length-scale with $L = 512$ m) does the parameterisation provide an acceptable fit for both cases.

The primary source of deviation lies in the constant-force assumption applied within the canopy, namely $\tau_{f;L}(z < h_{max}) \approx \tau_{0;L} \approx \langle \tau_{z;L} \rangle_{max}$. This assumption is adequate in the plane-averaged sense, that is, $L = \infty$, where variations in the cumulative forcing are negligible relative to its magnitude. However, within a local filter,

1477870x, 0, Downloaded from https://rmets.onlinelibrary.wiley.com/doi/10.1002/qj.70305 by Imperial College London, Wiley Online Library on [25/09/2026]. See the Terms and Conditions (https://onlinelibrary.wiley.com/terms-and-conditions) on Wiley Online Library for rules of use; OA articles are governed by the applicable Creative Commons License

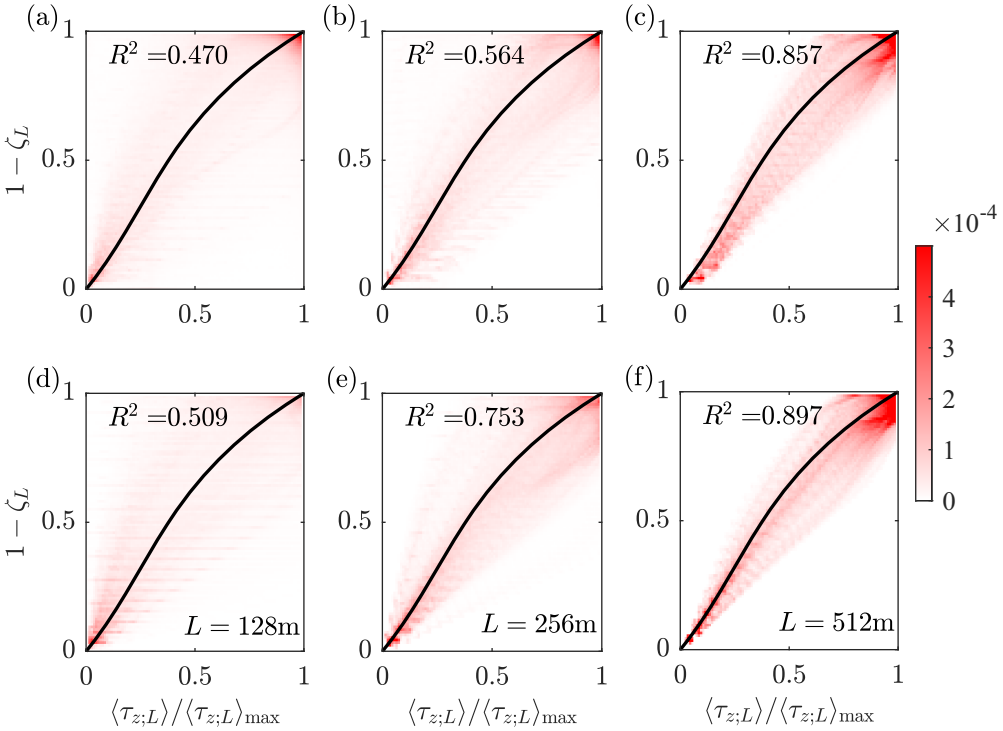


FIGURE 11 The distribution density of normalised local total kinematic stress $\langle\tau_{z;L}\rangle/\langle\tau_{z;L}\rangle_{\max}$ against the local scaled frontal area ζ_L at different averaging lengths: (a,d) $L = 128$ m, (b,e) $L = 256$ m, and (c,f) $L = 512$ m, for (top panel) CC and (bottom panel) SC, respectively. The solid line represents the parameterisation Equation (14) with modified constants $A = 0.89$, $B = 1.82$. The coefficient of determination R^2 is labelled to show the performance of the parameterisation. [Colour figure can be viewed at wileyonlinelibrary.com]

spatial variations in $\tau_{f;L}$ are no longer negligible relative to its mean, violating the constant-force approximation. Moreover, the neglected horizontal transport terms increase the discrepancy further as L decreases.

5 | CONCLUSIONS

A central question for next-generation urban canopy modelling is whether the standard assumption of horizontal homogeneity remains defensible as NWP grids approach hectometric resolution (Barlow, 2014; Lean *et al.*, 2024). At these scales, urban surfaces enter the so-called *building grey zone*, in which large buildings and the flow around them become partially resolved while smaller-scale variability does not, so that surface parameterisations become more complex rather than simpler and horizontal exchanges between adjacent cells become first-order (Lean *et al.*, 2024). This work addresses the question directly by providing a diagnostic, the characteristic urban length-scale ℓ of morphology-induced flow heterogeneity, that provides a reference for the length-scale of any given morphology at which resolved and unresolved heterogeneity become equally important. ℓ separates two distinct modelling regimes: at $L \gtrsim \ell$, the flow is sufficiently homogenised that conventional plane-averaged closures remain useful; at $L < \ell$, horizontal transport and filter-to-filter variability are first-order, and scale-aware (or heterogeneity-aware) formulations become necessary.

We obtained ℓ by applying the framework of van Reeuwijk and Huang (2025b), a 2-D horizontal coarse-graining filter that generates a series of coarser fields and quantifies the resolved and unresolved variances of the flow at each scale, to building-resolved LES of two layouts of the University of Bristol campus, the same site used in the ASSURE wind-tunnel programme (Bi *et al.*, 2025). In the disc configuration (CC), the buildings form an approximately circular cluster with large open spaces at the corners of the periodic patch; in the modified layout (SC), these corners are infilled with additional buildings. The diagnosed length-scale is strongly morphology-dependent: $\ell \approx 256$ m for CC, about one third of the domain size. This scale is comparable with the cluster radius and reflects neighbourhood-scale flow heterogeneity induced by the contrast between the built disc and the open corners, and is also consistent with the few-hundred-metre variability scale typically associated with urban morphology (Lean *et al.*, 2024). This scale is one that current kilometre-scale NWP cannot resolve and that even hectometric models would capture only partially. For SC, $\ell \approx 64$ m, the scale of individual buildings. This contrast arises because CC exhibits heterogeneity at both the building scale (associated with the dense central cluster) and the neighbourhood scale (associated with the open corners); averaging over several buildings therefore does not eliminate the larger-scale variability. Consequently, a substantially larger averaging length is required before the flow becomes approximately homogeneous across the filter. Infilling the corners in SC

1477870x, 0, Downloaded from https://rmets.onlinelibrary.wiley.com/doi/10.1002/qj.70305 by Imperial College London, Wiley Online Library on [25/09/2026]. See the Terms and Conditions (https://onlinelibrary.wiley.com/terms-and-conditions) on Wiley Online Library for rules of use; OA articles are governed by the applicable Creative Commons License

largely removes this neighbourhood-scale organisation, leaving the building scale as the dominant source of heterogeneity. Although based on two related morphologies, the fourfold contrast demonstrates for these two configurations that ℓ is not a universal property of cities but a layout-specific diagnostic that should be computed before any horizontally averaged closure is applied.

An a priori test of the distributed drag and turbulent-stress parameterisations of van Reeuwijk and Huang (2025b), with constants refitted to the present cases ($A = 0.89$, $B = 1.82$), confirms the role of ℓ as a transition scale. These parameterisations, derived from idealised morphologies under a horizontally homogeneous assumption, generally improve as L/ℓ increases but lose fidelity rapidly at finer scales, where the underlying assumption is violated and horizontal exchanges between cells can no longer be neglected. The drag parameterisation degrades more gracefully; the turbulent-stress parameterisation, which additionally invokes a constant-stress canopy assumption, fails earlier. The decline is steeper than that observed in idealised cuboid arrays, reflecting the much larger filter-to-filter variability of realistic layouts and helping to explain why parameterisations transferred unchanged from idealised studies often disappoint when applied to real cities.

The principal implication is that the resolution dependence of urban closures cannot be addressed without first asking what scale of heterogeneity the urban morphology actually contains. The framework employed offers a practical a priori tool to assess the scale awareness of urban parameterisations from building-resolving flow data and relating it to the underlying morphology, and provides a quantitative basis on which scale-aware closures, the form and coefficients of which adapt to L/ℓ, can be developed, addressing directly the call by Lean *et al.* (2024) for LES-based development of urban parameterisations on realistic geometries. A limitation of the present analysis could arise from the horizontal periodicity of the LES domain. Accordingly, the convolution filter is also applied periodically, with portions extending beyond one boundary wrapped to the opposite side. This treatment is consistent with the simulated flow and avoids arbitrary truncation of the filter near the domain boundaries. However, as the filter length approaches or exceeds half the domain width, neighbouring filter windows overlap strongly and sample the periodic continuation of the urban layout increasingly, making the filtered values increasingly correlated. Results at these scales therefore become more sensitive to the finite periodic domain, limiting their ability to represent morphology-dependent flow heterogeneity at comparable or larger scales. The remaining steps are to apply the diagnostic across a wider range of cities and local-climate-zone types, to extend it beyond neutral stability, and to translate it into operational closures that bridge kilometre-scale and hectometric NWP.

ACKNOWLEDGEMENTS

The support of the ARCHER2 UK National Supercomputing Service (project ARCHER2-eCSE05-3) and the NERC highlight grant ASSURE: Across-Scale ProcesseS in Urban Environment (NE/W002868/1) is acknowledged.

CONFLICT OF INTEREST STATEMENT

The authors report no conflict of interest.

DATA AVAILABILITY STATEMENT

The data that support the findings of this study are available from the corresponding author upon reasonable request.

ORCID

Jingzi Huang https://orcid.org/0000-0003-1668-1034
Maarten van Reeuwijk https://orcid.org/0000-0003-4840-5050

REFERENCES

Atar, L. & Mercan, O. (2026) Les of wind-induced pressures and flow structures around tandem buildings. *Journal of Wind Engineering and Industrial Aerodynamics*, 269, 106304. Available from: https://doi.org/10.1016/j.jweia.2025.106304

Auerswald, T., Klippel, K., Thomas, T.G. et al. (2024) Effect of flow variability on dispersion of continuous and puff releases in a regular street network. *Boundary-Layer Meteorology*, 190, 20. Available from: https://doi.org/10.1007/s10546-024-00863-z

Baldauf, M., Seifert, A., Förstner, J., Majewski, D., Raschendorfer, M. & Reinhardt, T. (2011) Operational convective-scale numerical weather prediction with the Cosmo model: description and sensitivities. *Monthly Weather Review*, 139(12), 3887–3905. Available from: https://doi.org/10.1175/MWR-D-10-05013.1 https://journals.ametsoc.org/view/journals/mwre/139/12/mwr-d-10-05013.1.xml

Barlow, J.F. (2014) Progress in observing and modelling the urban boundary layer. *Urban Climate*, 10, 216–240. Available from: https://doi.org/10.1016/j.uclim.2014.03.011, https://www.sciencedirect.com/science/article/pii/S2212095514000558 ICUC8: The 8th International Conference on Urban Climate and the 10th Symposium on the Urban Environment.

Bi, D., Carpentieri, M., Placidi, M. & Robins, A. (2025) Wind tunnel modelling of flow and pollutant dispersion in a heterogeneous urban area. In: *12th International Conference on Urban Climate (ICUC12)*. Rotterdam, The Netherlands: Copernicus Publications. Available from: https://doi.org/10.5194/icuc12-1014 ICUC12-1014.

Blunn, L., Coceal, O., Nazarian, N., Barlow, J., Plant, B., Bohnenstengel, S. et al. (2022) Turbulence characteristics across a range of idealized urban canopy geometries. *Boundary-Layer Meteorology*, 182, 275–307. Available from: https://doi.org/10.1007/s10546-021-00658-6 https://centaur.reading.ac.uk/99701/

Bryan, G.H., Wyngaard, J.C. & Fritsch, J.M. (2003) Resolution requirements for the simulation of deep moist convection.

1477870x, 0, Downloaded from https://rmets.onlinelibrary.wiley.com/doi/10.1002/qj.70305 by Imperial College London, Wiley Online Library on [25/09/2026]. See the Terms and Conditions (https://onlinelibrary.wiley.com/terms-and-conditions) on Wiley Online Library for rules of use; OA articles are governed by the applicable Creative Commons License

Monthly Weather Review, 131(10), 2394–2416. Available from: https://doi.org/10.1175/1520-0493(2003)131<2394:RRFTSO>2.0.CO;2, https://journals.ametsoc.org/view/journals/mwre/131/10/1520-0493_2003_131_2394_rrftso_2.0.co_2.xml

Chen, S. & Dipankar, A. (2022) On the applicability of urban canopy parametrization in building grey zone. *Quarterly Journal of the Royal Meteorological Society*, 148(745), 1644–1662. Available from: https://doi.org/10.1002/qj.4269

Cheng, W.C. & Yang, Y. (2023) Scaling of flows over realistic urban geometries: a large-eddy simulation study. *Boundary-Layer Meteorology*, 186, 125–144.

Clements, D., Coburn, M., Cox, S.J., Bulot, F.M.J., Xie, Z.T. & Vanderwel, C. (2024) Comparing large-eddy simulation and Gaussian plume model to sensor measurements of an urban smoke plume. *Atmosphere*, 15(9), https://www.mdpi.com/2073-4433/15/9/1089, 1089.

Coburn, M., Xie, Z.T. & Herring, S.J. (2022) Numerical simulations of boundary-layer airflow over pitched-roof buildings. *Boundary-Layer Meteorology*, 185, 415–442. Available from: https://doi.org/10.1007/s10546-022-00738-1

Coceal, O. & Belcher, S.E. (2004) A canopy model of mean winds through urban areas. *Quarterly Journal of the Royal Meteorological Society*, 130(599), 1349–1372. Available from: https://doi.org/10.1256/qj.03.40

Coceal, O., Thomas, T.G., Castro, I.P. & Belcher, S.E. (2006) Mean flow and turbulence statistics over groups of urban-like cubical obstacles. *Boundary-Layer Meteorology*, 121(3), 491–519.

Ding, S.S., Placidi, M., Carpentieri, M. et al. (2023) Neutrally- and stably-stratified boundary layers adjustments to a step change in surface roughness. *Experiments in Fluids*, 64, 86. Available from: https://doi.org/10.1007/s00348-023-03626-7

Fellini, S., Majumdar, D., Salizzoni, P. & van Reeuwijk, M. (2026) Three-dimensional pollutant dispersion in tree-lined urban canyons: combined wind-tunnel and les analysis. *Atmospheric Environment*, 367, 121748. Available from: https://doi.org/10.1016/j.atmosenv.2025.121748 https://www.sciencedirect.com/science/article/pii/S135223102500723X

Finnigan, J. (2000) Turbulence in plant canopies. *Annual Review of Fluid Mechanics*, 32, 519–571. Available from: https://doi.org/10.1146/annurev.fluid.32.1.519

Giometto, M., Christen, A., Meneveau, C., Fang, J., Krafczyk, M. & Parlange, M. (2016) Spatial characteristics of roughness sublayer mean flow and turbulence over a realistic urban surface. *Boundary-Layer Meteorology*, 160(3), 425–452. Available from: https://doi.org/10.1007/s10546-016-0157-6

Kanda, M., Kawai, T., Kanega, M., Moriwaki, R., Narita, K. & Hagishima, A. (2005) A simple energy balance model for regular building arrays. *Boundary-Layer Meteorology*, 116(3), 423–443. Available from: https://doi.org/10.1007/s10546-004-7956-x

Kusaka, H., Ikeda, R., Sato, T., Iizuka, S. & Boku, T. (2024) Development of a multi-scale meteorological large-eddy simulation model for urban thermal environmental studies: the "city-les" model version 2.0. *Journal of Advances in Modeling Earth Systems*, 16(10), e2024MS004367. Available from: https://doi.org/10.1029/2024MS004367

Kusaka, H., Kondo, H., Kikegawa, Y. & Kimura, F. (2001) A simple single-layer urban canopy model for atmospheric models: comparison with multi-layer and slab models. *Boundary-Layer Meteorology*, 101(3), 329–358. Available from: https://doi.org/10.1023/A:1019207923078

Lean, H.W., Theeuwes, N.E., Baldauf, M., Barkmeijer, J., Bessardon, G., Blunn, L. et al. (2024) The hectometric modelling challenge: gaps in the current state of the art and ways forward towards the implementation of 100-m scale weather and climate models. *Quarterly Journal of the Royal Meteorological Society*, 150(765), 4671–4708. Available from: https://doi.org/10.1002/qj.4858

Lim, H.D., Hertwig, D., Grylls, T., Gough, H., van Reeuwijk, M., Grimmond, S. et al. (2022) Pollutant dispersion by tall buildings: laboratory experiments and large-Eddy simulation. *Experiments in Fluids*, 63(6), 92. Available from: https://doi.org/10.1007/s00348-022-03439-0

Lipson, M.J., Grimmond, S., Best, M., Abramowitz, G., Coutts, A., Tapper, N. et al. (2024) Evaluation of 30 urban land surface models in the urban-plumber project: phase 1 results. *Quarterly Journal of the Royal Meteorological Society*, 150(758), 126–169. Available from: https://doi.org/10.1002/qj.4589

Lu, J., Nazarian, N., Hart, M.A., Krayenhoff, E.S. & Martilli, A. (2024) A one-dimensional urban flow model with an eddy-diffusivity mass-flux (edmf) scheme and refined turbulent transport (mlucm v3.0). *Geoscientific Model Development*, 17(7), 2525–2545. Available from: https://doi.org/10.5194/gmd-17-2525-2024

Ludwig, S., Plein, M., Barlow, J.F., Escobar-Ruiz, V., Grimmond, S., Matthews, J. et al. (2025) Street-level weather station network in Bristol, UK: Station documentation (1.0). https://doi.org/10.5281/zenodo.15537606

Macdonald, R., Griffiths, R. & Hall, D. (1998) An improved method for the estimation of surface roughness of obstacle arrays. *Atmospheric Environment*, 32(11), 1857–1864. Available from: https://doi.org/10.1016/S1352-2310(97)00403-2 https://www.sciencedirect.com/science/article/pii/S1352231097004032

Martilli, A., Clappier, A. & Rotach, M. (2002) An urban surface exchange parameterisation for mesoscale models. *Boundary-Layer Meteorology*, 104, 261–304. Available from: https://doi.org/10.1023/A:1016099921195

Masson, V., Heldens, W., Bocher, E., Bonhomme, M., Bucher, B., Burmeister, C. et al. (2020) City-descriptive input data for urban climate models: model requirements, data sources and challenges. *Urban Climate*, 31, 100536. Available from: https://doi.org/10.1016/j.uclim.2019.100536 https://www.sciencedirect.com/science/article/pii/S2212095518303663

Nazarian, N., Krayenhoff, E.S. & Martilli, A. (2020) A one-dimensional model of turbulent flow through "urban" canopies (mlucm v2.0): updates based on large-eddy simulation. *Geoscientific Model Development*, 13(3), 937–953. Available from: https://doi.org/10.5194/gmd-13-937-2020

Nepf, H.M. (2012) Flow and transport in regions with aquatic vegetation. *Annual Review of Fluid Mechanics*, 44, 123–142. Available from: https://doi.org/10.1146/annurev-fluid-120710-101048

Owens, S.O., Majumdar, D., Wilson, C.E., Bartholomew, P. & van Reeuwijk, M. (2024) A conservative immersed boundary method for the multi-physics urban large-eddy simulation model udales v2.0. *EGUsphere*, 2024, 1–33. Available from: https://doi.org/10.5194/egusphere-2024-96 https://egusphere.copernicus.org/preprints/2024/egusphere-2024-96/

Pope, S.B. (2000) *Turbulent flows*. Cambridge: Cambridge University Press. Available from: https://doi.org/10.1017/CBO9780511840531

Raupach, M.R. & Shaw, R.H. (1982) Averaging procedures for flow within vegetation canopies. *Boundary-Layer Meteorology*, 22, 79–90.

1477870x, 0, Downloaded from https://rmets.onlinelibrary.wiley.com/doi/10.1002/qj.70305 by Imperial College London, Wiley Online Library on [25/09/2026]. See the Terms and Conditions (https://onlinelibrary.wiley.com/terms-and-conditions) on Wiley Online Library for rules of use; OA articles are governed by the applicable Creative Commons License

Santiago, J.L. & Martilli, A. (2010) A dynamic urban canopy parameterization for mesoscale models based on computational fluid dynamics Reynolds-averaged Navier-stokes microscale simulations. *Boundary-Layer Meteorology*, 137(3), 417–439. Available from: https://doi.org/10.1007/s10546-010-9538-4

Schlichting, H. & Gersten, K. (2017) *Boundary-layer theory*. Heidelberg, ISBN 978–3–662-52917-1: Springer Berlin. Available from: https://doi.org/10.1007/978-3-662-52919-5

Schmid, M., Lawrence, G.A., Parlange, M.B. & Giometto, M.G. (2019) Volume averaging for urban canopies. *Boundary-Layer Meteorology*, 173, 349–372.

Smagorinsky, J. (1963) General circulation experiments with the primitive equations. I. The basic experiment. *Monthly Weather Review*, 91(3), 99–164. Available from: https://doi.org/10.1175/1520-0493(1963)091<0099:GCEWTP>2.3.CO;2

Stewart, I.D. & Oke, T.R. (2012) Local climate zones for urban temperature studies. *Bulletin of the American Meteorological Society*, 93(12), 1879–1900. Available from: https://doi.org/10.1175/BAMS-D-11-00019.1 https://journals.ametsoc.org/view/journals/bams/93/12/bams-d-11-00019.1.xml

Suter, I., Grylls, T., Sützl, B.S., Owens, S.O., Wilson, C.E. & van Reeuwijk, M. (2022) Udales 1.0: a large-eddy simulation model for urban environments. *Geoscientific Model Development*, 15(13), 5309–5335. Available from: https://doi.org/10.5194/gmd-15-5309-2022 https://gmd.copernicus.org/articles/15/5309/2022/

Sützl, B.S., Rooney, G.G., Finnenkoetter, A., Bohnenstengel, S.I., Grimmond, S. & van Reeuwijk, M. (2021) Distributed urban drag parametrization for sub-kilometre scale numerical weather prediction. *Quarterly Journal of the Royal Meteorological Society*, 147(741), 3940–3956.

Sützl, B.S., Rooney, G.G. & van Reeuwijk, M. (2020) Drag distribution in idealized heterogeneous urban environments. *Boundary-Layer Meteorology*, 178, 225–248.

Tang, Y., Lean, H.W. & Bornemann, J. (2013) The benefits of the met office variable resolution NWP model for forecasting convection. *Meteorological Applications*, 20(4), 417–426. Available from: https://doi.org/10.1002/met.1300

Uno, I., Cai, X.M., Steyn, D.G. & Emori, S. (1995) A simple extension of the Louis method for rough surface layer modelling. *Boundary-Layer Meteorology*, 76, 395–409.

van Reeuwijk, M. & Huang, J. (2025a) Dataset for "multi-scale analysis of flow over heterogeneous urban environments". https://doi.org/10.5281/zenodo.17102845

van Reeuwijk, M. & Huang, J. (2025b) Multi-scale analysis of flow over heterogeneous urban environments. *Boundary-Layer Meteorology*, 191(11), 47.

Van Reeuwijk, M., Vassilicos, J.C. & Craske, J. (2021) Unified description of turbulent entrainment. *Journal of Fluid Mechanics*, 908, A12. Available from: https://doi.org/10.1017/jfm.2020.836

Vreman, A.W. (2004) An eddy-viscosity subgrid-scale model for turbulent shear flow: algebraic theory and applications. *Physics of Fluids*, 16(10), 3670–3681. Available from: https://doi.org/10.1063/1.1785131

Whitaker, S. (1999) The method of volume averaging. In: *Theory and applications of transport in porous media*. Dordrecht, Boston: Kluwer Academic Publishers.

Xie, Z.T. & Castro, I.P. (2006) Les and rans for turbulent flow over arrays of wall-mounted obstacles. *Flow, Turbulence and Combustion*, 76(3), 291–312. Available from: https://doi.org/10.1007/s10494-006-9018-6

Xie, Z.T., Coceal, O. & Castro, I.P. (2008) Large-eddy simulation of flows over random urban-like obstacles. *Boundary-Layer Meteorology*, 129, 1–23.

Yu, T., Sützl, B.S. & van Reeuwijk, M. (2023) Urban neighbourhood classification and multi-scale heterogeneity analysis of greater London. *Environment and Planning B: Urban Analytics and City Science*, 50(6), 1534–1558. Available from: https://doi.org/10.1177/23998083221140890

How to cite this article: Huang, J. & van Reeuwijk, M. (2026) Multi-scale flow analysis for scale-aware urban canopy models. *Quarterly Journal of the Royal Meteorological Society*, e70305. Available from: https://doi.org/10.1002/qj.70305

APPENDIX A. COMPUTATIONAL DETAILS

The convolution in Equation (1) can be computed efficiently using two-dimensional fast Fourier transforms (2-D FFTs). For ease of implementation, the equation can be rewritten by introducing a fluid mask I_f (1 in the fluid region and 0 in the solid), which extends the integral over the fluid region to the entire plane $\Omega(z)$:

$$\langle\varphi\rangle_L(\boldsymbol{x}) = \int_{\Omega(z)} \mathcal{A}(\boldsymbol{x}_h - \boldsymbol{y}_h) I_f(\boldsymbol{y}_h, z)\varphi(\boldsymbol{y}_h, z)\, \mathrm{d}\boldsymbol{y}_h. \tag{A1}$$

Specifically, the horizontal FFTs of φ and the kernel $\mathcal{A}$ are computed first. Their product is then transformed back to physical space via the inverse FFT, yielding the filtered field at all horizontal points simultaneously. This approach reduces computational cost from direct spatial convolution to approximately $\mathcal{O}((\log n)^2 n^3)$ operations for a cubic domain of size n^3, which is particularly beneficial for large domains and large filter lengths. The computational details are described by van Reeuwijk and Huang (2025a).

A key feature of urban Dutch Atmospheric Large Eddy Simulation (uDALES) is its ability to represent solid surfaces through a facet mesh using the immersed boundary method. Each facet, denoted m, is associated with a Cartesian grid cell at indices (I_m, J_m, K_m). A surface quantity ϕ_m on facet m with area A_m can thus be mapped to a volumetric density field ρ_ϕ, which is non-zero only in the cells adjacent to the surface boundary. In discrete form,

$$\rho_{\phi;ijk} = \sum_{m \in M_{ijk}} \frac{\phi_m A_m}{\Delta x \Delta y \Delta z_{K_m}}, \tag{A2}$$

1477870x, 0, Downloaded from https://rmets.onlinelibrary.wiley.com/doi/10.1002/qj.70305 by Imperial College London, Wiley Online Library on [25/09/2026]. See the Terms and Conditions (https://onlinelibrary.wiley.com/terms-and-conditions) on Wiley Online Library for rules of use; OA articles are governed by the applicable Creative Commons License

where M_{ijk} is the set of all facets associated with Cartesian cell (i, j, k). This mapping allows surface fluxes to be incorporated consistently into the LES framework.

Integration over the solid–fluid interface then provides the total flux exchanged across the boundary. The resulting volumetric field can then be filtered straightforwardly as

$$\left\langle \rho_\phi \right\rangle(\boldsymbol{x}) = \int_{\Omega_\mathrm{f}} \mathcal{A}(\boldsymbol{x}_h - \boldsymbol{y}_h)\rho_\phi(\boldsymbol{y}_h)\ \mathrm{d}\boldsymbol{y}_h. \tag{A3}$$

The distributed drag term $\langle f_\mathrm{D} \rangle$ can be evaluated by choosing $\phi_m = -(\overline{p}_m \boldsymbol{e}_x - \nu(\nabla \overline{u})_m) \cdot \boldsymbol{N}_m$, which includes the surface pressure (form drag) and viscous shear stress (skin drag) contributions in the streamwise direction. Denoting the volumetric drag density by ρ_D, we have $\langle f_\mathrm{D} \rangle = \langle \rho_\mathrm{D} \rangle$.

The frontal area density can be evaluated by setting $\phi_m = -\min(\boldsymbol{e}_u \cdot \boldsymbol{N}_m, 0)$, where e_u is the unit vector of the local velocity. This yields a frontal-area density field ρ_L such that $\int \rho_L\ \mathrm{d}x\ \mathrm{d}y = L_\mathrm{b}$ and $\int \rho_L\ \mathrm{d}V = A_\mathrm{F}$. Recall that L_b is the frontal building width. From this, the filter-dependent cumulative normalised frontal-area index is defined as

$$\zeta_L(\boldsymbol{x}_h, z) = \frac{1}{\lambda_{\mathrm{f};L}} \int_z^h \langle \rho_L \rangle_L(\boldsymbol{x}_h, z')\ \mathrm{d}z', \tag{A4}$$

with

$$\lambda_{\mathrm{f};L}(\boldsymbol{x}_h) = \int_0^h \langle \rho_L \rangle_L(\boldsymbol{x}_h, z')\ \mathrm{d}z'. \tag{A5}$$

1477870x, 0, Downloaded from https://rmets.onlinelibrary.wiley.com/doi/10.1002/qj.70305 by Imperial College London, Wiley Online Library on [25/09/2026]. See the Terms and Conditions (https://onlinelibrary.wiley.com/terms-and-conditions) on Wiley Online Library for rules of use; OA articles are governed by the applicable Creative Commons License